Monthly Notices
of the
ROYAL ASTRONOMICAL SOCIETY

MNRAS **479,** 4172–4186 (2018)
Advance Access publication 2018 June 28

doi:10.1093/mnras/sty1694

The intrinsic three-dimensional shape of galactic bars

J. Méndez-Abreu,[1,2]★ L. Costantin,[3] J. A. L. Aguerri,[1,2] A. de Lorenzo-Cáceres[1,2] and E. M. Corsini[3,4]

[1]*Instituto de Astrofísica de Canarias, Calle Vía Láctea s/n, E-38205 La Laguna, Tenerife, Spain*
[2]*Departamento de Astrofísica, Universidad de La Laguna, E-38200 La Laguna, Tenerife, Spain*
[3]*Dipartimento di Fisica e Astronomia 'G. Galilei', Universitá di Padova, vicolo dell'Osservatorio 3, I-35122 Padova, Italy*
[4]*INAF-Osservatorio Astronomico di Padova, vicolo dell'Osservatorio 5, I-35122 Padova, Italy*

Accepted 2018 June 25. Received 2018 June 24; in original form 2018 January 15

ABSTRACT

We present the first statistical study on the intrinsic three-dimensional (3D) shape of a sample of 83 galactic bars extracted from the CALIFA survey. We use the galaXYZ code to derive the bar intrinsic shape with a statistical approach. The method uses only the geometric information (ellipticities and position angles) of bars and discs obtained from a multicomponent photometric decomposition of the galaxy surface-brightness distributions. We find that bars are predominantly prolate-triaxial ellipsoids (68 per cent), with a small fraction of oblate-triaxial ellipsoids (32 per cent). The typical flattening (intrinsic *C*/*A* semiaxis ratio) of the bars in our sample is 0.34, which matches well the typical intrinsic flattening of stellar discs at these galaxy masses. We demonstrate that, for prolate-triaxial bars, the intrinsic shape of bars depends on the galaxy Hubble type and stellar mass (bars in massive S0 galaxies are thicker and more circular than those in less massive spirals). The bar intrinsic shape correlates with bulge, disc, and bar parameters. In particular with the bulge-to-total (*B*/*T*) luminosity ratio, disc $g - r$ colour, and central surface brightness of the bar, confirming the tight link between bars and their host galaxies. Combining the probability distributions of the intrinsic shape of bulges and bars in our sample, we show that 52 per cent (16 per cent) of bulges are thicker (flatter) than the surrounding bar at 1σ level. We suggest that these percentages might be representative of the fraction of classical and disc-like bulges in our sample, respectively.

Key words: galaxies: evolution – galaxies: formation – galaxies: photometry – galaxies: structure.

1 INTRODUCTION

Stellar bars are common structures in disc galaxies in the nearby Universe (Marinova & Jogee 2007; Barazza, Jogee & Marinova 2008; Aguerri, Méndez-Abreu & Corsini 2009) and they are considered the main internal mechanism driving the dynamical and secular evolution of disc galaxies (Kormendy & Kennicutt 2004). The presence of a bar is able to modify the external appearance of a galaxy, changing its structure and morphology within the central ∼10 kpc. Numerical simulations have found that stellar bars redistribute the angular momentum between the baryonic and dark matter components (Debattista & Sellwood 1998, 2000). The relative amount of exchanged angular momentum is related to specific properties of the galaxies, such as the bar mass, halo density, and halo velocity dispersion (Athanassoula 2003; Sellwood & Debattista 2006; Athanassoula, Machado & Rodionov 2013). In addition, bars are able to funnel material towards the galaxy centre where starbursts can ignite (Shlosman, Begelman & Frank 1990; Sheth et al. 2005), and they have been proposed as an efficient mechanism to create new structures in the galaxy centres such as disc-like bulges (Kormendy & Kennicutt 2004), inner star-forming rings (Buta, Byrd & Freeman 2003; Muñoz-Tuñón, Caon & Aguerri 2004), and inner bars (Erwin 2004; Debattista & Shen 2007; de Lorenzo-Cáceres, Falcón-Barroso & Vazdekis 2013). Therefore, understanding the mechanisms leading to the formation of bars is key to understand galaxy evolution in general.

The observed properties of stellar bars, and their relation with the characteristics of the host galaxies have been extensively reviewed in the literature. It is now established that the main driver for the presence of a bar is the galaxy mass (Méndez-Abreu et al. 2010; Nair & Abraham 2010; Erwin 2017), with the bar frequency reaching a peak at $M_\star \sim 10^{9.5}\mathrm{M}_\odot$ (Méndez-Abreu et al. 2012) and quickly declining towards both lower and higher masses. Many observational and theoretical studies have also investigated other internal and external galaxy properties to understand which

★ E-mail: jairomendezabreu@gmail.com

galaxies are more or less likely to host bars obtaining some contradictory results (Barazza et al. 2009; Athanassoula et al. 2013; Díaz-García et al. 2016; Martinez-Valpuesta et al. 2017). In Aguerri et al. (2009), we found that red, massive, gas-poor galaxies host less and shorter bars than blue, low-mass, and gas-rich galaxies. These results were similar to those presented in Barazza et al. (2008) and Nair & Abraham (2010). However, other authors obtained completely opposite results (Masters et al. 2011; Skibba et al. 2012; Consolandi 2016). In Méndez-Abreu et al. (2012), we discussed that most of these discrepancies might be solved if galaxy samples would have been carefully selected in both stellar mass and environment to avoid biases when dealing with bar statistics. Recently, Erwin (2017) confirmed this argumentation and he also pointed out the problems of dealing with poor spatial resolution when analysing galaxy bars.

Despite the tremendous progress in the field, an important piece of information is still hidden in the intrinsic three-dimensional (3D) structure of stellar bars, and how the bar shape is related to the different galaxy properties. *N*-body simulations have demonstrated how the 3D structure of stellar bars is strongly dependent on the time since bar formation. Bars form spontaneously in self-gravitating rotating galactic discs (Combes et al. 1990; Debattista & Sellwood 2000; Athanassoula 2003); initially they have a thin vertical density profile similar to that of the disc, i.e. bars are formed by the re-arrangement of disc material (Athanassoula et al. 2013). This scenario has been confirmed by orbital analysis where planar and circular orbits become more elongated and material gets trapped around the stable periodic orbits of the x1 family (Contopoulos & Papayannopoulos 1980; Athanassoula et al. 1983; Athanassoula 1992). However, this configuration quickly changes due to the bar buckling out of the disc plane, which modifies the vertical structure of the bar inner regions and it creates a substantially thicker component than the surrounding disc (Combes & Sanders 1981; Raha et al. 1991; Martinez-Valpuesta, Shlosman & Heller 2006). This vertical structure, which appears as boxy- or peanut-shaped when the galaxy is seen edge-on, has also been demonstrated to be part of the bar through 3D orbital analysis (Skokos, Patsis & Athanassoula 2002). In summary, numerical simulations suggest that, in the long term, most bars should be formed by an inner thick component and an outer part thinner than the inner region (Athanassoula 2005).

Observationally, boxy/peanut (B/P) shaped bars have been detected in many studies of edge-on and, indirectly, also in face-on galaxies (Lütticke, Dettmar & Pohlen 2000; Méndez-Abreu et al. 2008; Erwin & Debattista 2013; Yoshino & Yamauchi 2015; Ciambur & Graham 2016). However, they have not been generally included as a separate component in either photometric decompositions (but see Laurikainen & Salo 2016, and references therein) or bar deprojection schemes (Martin 1995; Gadotti et al. 2007). In fact, Zou, Shen & Li (2014) using numerical simulations to test their 2D bar deprojection method concluded that, to first-order approximation, one-ellipsoid models could represent the 3D structure of the bar reasonably well. This was also pointed out in early hydrodnamical simulations of barred galaxies (Hunter et al. 1988; England 1989; Aguerri, Balcells & Peletier 2001a). In addition, the peanut shape generally does not encompass the full extent of the bar, i.e. there is some flat bar outside the buckled inner part (Lütticke et al. 2000; Méndez-Abreu et al. 2008). Erwin & Debattista (2013) also argue that not every bar thickens vertically and estimated that at least 13 per cent of bars in galaxies have not buckled.

In this paper, we present the first statistical study of the intrinsic shape of stellar bars using the observed sample of the Calar Alto Legacy Integral Field Area survey Data Release 3 (CALIFA-DR3 Sánchez et al. 2016). We use the galaXYZ code described in Méndez-Abreu et al. (2010) and Costantin et al. (2018) and compare the bar intrinsic shape with other observed galaxy properties to shed light on the formation of these structures. To this aim, we consider bars to be, at first order, single triaxial ellipsoids. Despite the limitations of such a description, it is an appropriate starting point to study in a quantitative way the 3D shape of bars with respect to galaxy properties. The paper is organized as follows: Section 2 describes the sample of galaxies used in this work. Section 3 details the methodology to derive the intrinsic shape of stellar bars from their projected photometric properties. Section 4 describes the main results of this paper about the intrinsic shape of bars and its relation with other galaxy properties. The discussion of the results in the context of bar formation is also done in Section 4. The conclusions are given in Section 5. Throughout the paper, we assume a flat cosmology with $\Omega_{\rm m} = 0.3$, $\Omega_{\Lambda} = 0.7$, and a Hubble constant $H_0 = 70\,{\rm km\,s^{-1}\,Mpc^{-1}}$.

2 CALIFA SAMPLE OF BARRED GALAXIES

The sample of barred galaxies was selected from Méndez-Abreu et al. (2017). They present a two-dimensional multicomponent photometric decomposition of 404 galaxies from the CALIFA-DR3 (Sánchez et al. 2016). They represent all galaxies with either no clear signs of interaction or not strongly inclined within the 667 galaxies observed in the final CALIFA data release. They found 162 barred galaxies out of 404 galaxies. Following Costantin et al. (2018), we impose an inclination constraint to galaxies with $25^\circ < \theta < 65^\circ$. This assures the robustness of our method to derive the intrinsic shape of our bar sample. We ended up with 125 barred galaxies meeting this criterion. We further discarded 42 galaxies for the following reasons: i) galaxies with complex morphology in the outer parts of the discs, e.g. strong spiral arms or asymmetric discs, that make it difficult to deriving their geometric (ellipticity and position angle) properties (14 galaxies), ii) galaxies with very low surface brightness discs ($\mu_0 > 21\,{\rm mag\,arcsec^{-2}}$) or bars ($\mu_{0,\rm bar} > 22.5\,{\rm mag\,arcsec^{-2}}$) making it difficult to measure their geometry (eight galaxies), iii) galaxy discs for which the ellipticity and/or position angle from the photometric decomposition does not match the outer values of the corresponding radial profiles derived from the isophotal analysis (nine galaxies), iv) galaxies with an offcentred bar (three galaxies), and v) galaxies for which the uncertainties in the derived intrinsic shape (*B*/*A* or *C*/*A*) are larger than 1 (eight galaxies). The final sample amounts to 83 galaxies.

Méndez-Abreu et al. (2017) carried out the photometric decomposition analysis using the *g*-, *r*-, and *i*-band images. In this work, we have used the results from the *i*-band images to better resolve the bar component minimizing the dust effects with respect to the other SDSS passbands. The average *i*-band point spread function (PSF) full width at half maximum (FWHM) of the images is 1.1 ± 0.2 arcsec with a typical depth of $\mu_i \sim 26\,{\rm mag\,arcsec^{-2}}$. An example of the 2D photometric decomposition for NGC 5602 is shown in Fig. 1. The galaxies main properties (i.e. Hubble-type *HT*, stellar mass $M_\star$, Sérsic index parameter n, and bar radius $r_{\rm bar}$) from Méndez-Abreu et al. (2017) and Walcher et al. (2014) are shown in Fig. 2.

3 BARS INTRINSIC SHAPE

The derivation of the intrinsic shape of the individual bars in our sample was performed using the galaXYZ code. This method has previously been applied to the analysis of the intrinsic 3D shape of galactic bulges (Méndez-Abreu et al. 2010; Costantin et al. 2018).

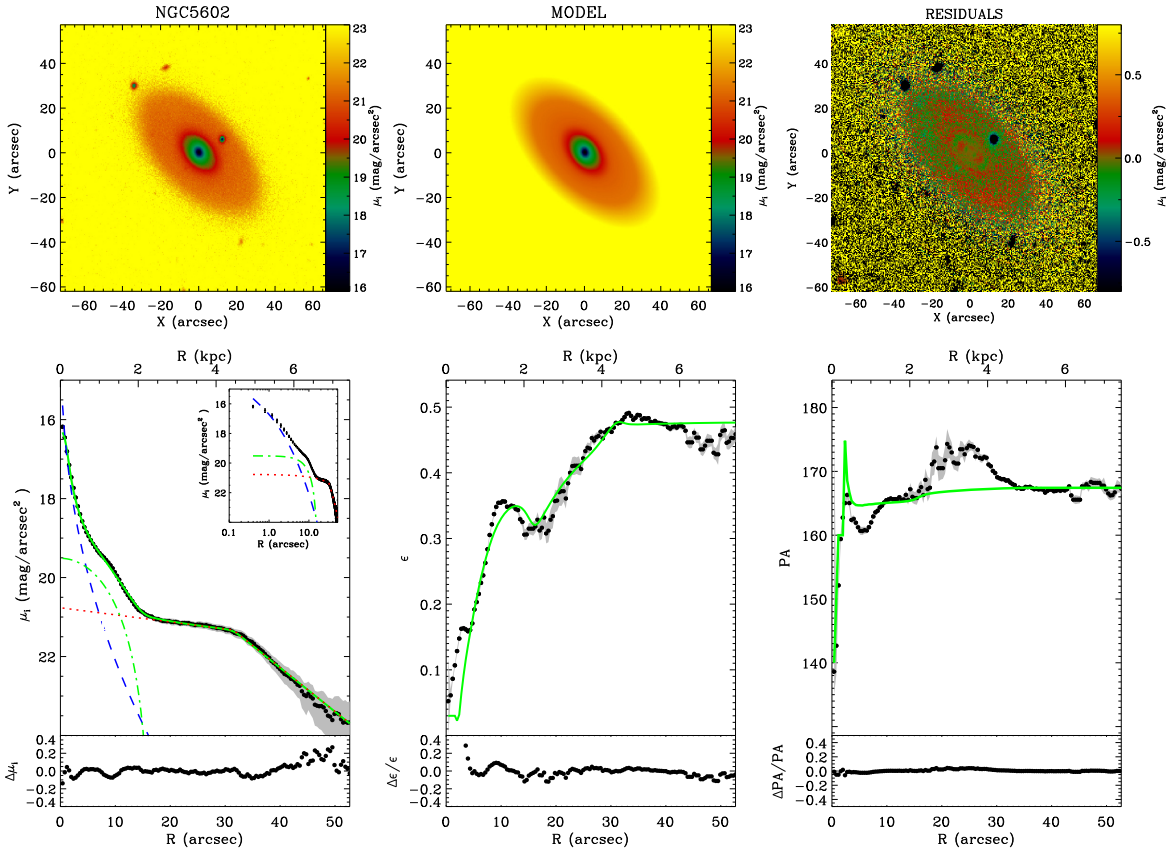

Figure 1. Example of the 2D photometric decomposition analysis for NGC 5602. The figure shows the best fit obtained using three components (bulge, bar, and truncated disc) for the *i* band. Top left panel: galaxy image. Top middle panel: best-fitting model of the galaxy image. Top right panel: residual image obtained by subtracting the best-fit model from the galaxy image. Bottom left panel: ellipse-averaged surface brightness radial profile of the galaxy (black dots) and best-fit model (cyan solid line). The light contributions of the bulge (dashed red line), disc (dotted blue line), and bar (dotted-dashed green line) are shown. The upper inset shows a zoom of the surface-brightness data and fit with a logarithmic scale for the distance to the centre of the galaxy. 1D surface brightness residuals (in mag arcsec^{-2} units) are shown in the bottom subpanel. Bottom middle panel: ellipse-averaged radial profile of ellipticity of the galaxy (black dots) and best-fit model (cyan solid line). 1D residuals (in percentage) are shown in the bottom subpanel. Bottom right panel: ellipse-averaged radial profile of position angle of the galaxy (black dots) and best-fit model (cyan solid line). 1D residuals (in percentage) are shown in the bottom subpanel. The grey shaded areas in the bottom panels represent the measurement errors derived from the `ellipse IRAF` task when applied to the galaxy image.

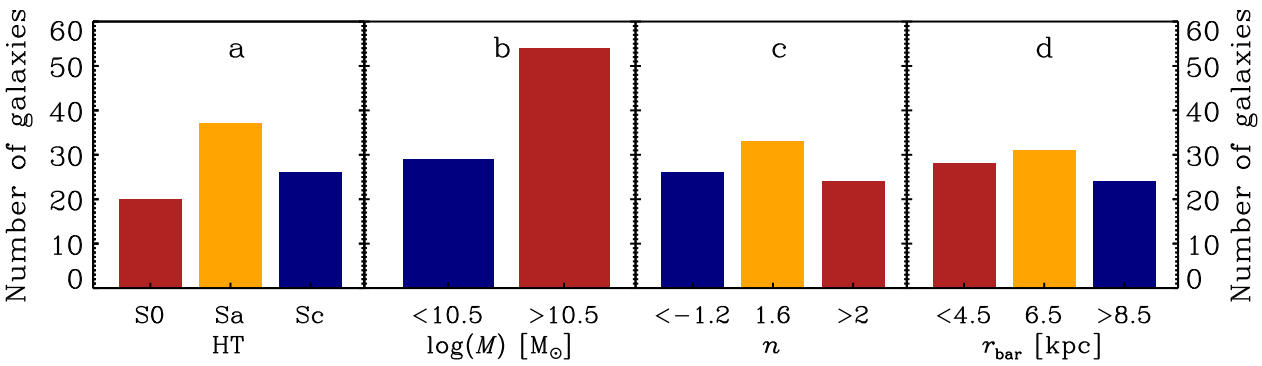

Figure 2. Distribution of the galaxy Hubble type (panel a; Sa bin comprises Sa–Sab–Sb galaxies, while Sc bin comprises Sbc–Scd–Sd–Sdm galaxies), stellar mass (panel b), Sérsic index of the bulge (panel c), and bar radius (panel d). The galaxy properties are taken from Méndez-Abreu et al. (2017) and Walcher et al. (2014).

However, it is worth noticing that our statistical approach is applicable to any galactic structure if the initial assumptions are fulfilled.

For the sake of clarity, we describe here the main hypotheses of our method. In order to characterize the intrinsic shape of a bar, we first assumed that it can be successfully modelled by a triaxial ellipsoid that shares the same equatorial plane as the disc. Secondly, the galaxy disc is considered to be an oblate ellipsoid with an intrinsic thickness given by a normal distribution function with mean intrinsic axial ratio $q_{0,d} = 0.267$ and standard deviation $\sigma_{q_{0,d}} = 0.102$ (Rodríguez & Padilla 2013). Moreover, a third condition imposes

that the bar and disc share the same centre, which coincides with the galaxy centre. This condition is also imposed in the photometric decomposition where all components are forced to share the same centre. We also visually checked the individual galaxies to look for offcentred bars such as those presented in Kruk et al. (2017) finding only 3 out of 125. This low fraction of offcentred bars is in agreement with the findings of Kruk et al. (2017) that most of these systems are located in low-mass galaxies. They were removed from the sample (see Section 2).

Regarding the first hypothesis, we discussed in Section 1 about the possibility of bars being comprised of both an inner vertically thick component (usually associated to the presence of a B/P structure) and another more extended and thinner bar. In our photometric decomposition, the inner B/P structure is not included as a different analytical component, and we visually checked all the fits to assure the external bar is fitted. We thus consider our intrinsic shape results to be representative of the outer extended bar. However, the presence of a B/P structure might still be affecting the measurements of the geometric parameters involved in our analysis of the 3D shape, i.e. the bar and disc ellipticities and position angles. To better quantify the effect of possible B/P structures in our sample, we carried out a visual classification of our sample galaxies in order to detect the possible presence of inner B/P structures. We followed the criteria established in a series of papers by Laurikainen et al. (2011); Athanassoula et al. (2015); Laurikainen & Salo (2017): a potential B/P is detected based on the presence of a close to circular isophotal contour in the central part of the bar with smaller ellipticity compared to the outer bar. In addition, we also used the criteria proposed by Erwin & Debattista (2013, 2017) to detect B/P structures. This is based on the presence of boxy isophotes in the inner part of the bar, accompanied by narrow, and offset with respect to the major axis, isophotes in the outer bar. These features are called spurs. A good example of the two types of projections expected for B/P structures is given in fig. 1 of Li, Ho & Barth (2017). Using this classification scheme, we found that 22 and 8 galaxies were classified as barlenses or possible barlenses (barlens?), respectively. Similarly, we found that 3 and 3 galaxies were classified as B/P or possible B/P (B/P?), respectively. Finally, we classified 47 galaxies as not presenting any characteristic of an inner B/P structure. The classification for each galaxy is shown in Table A1. Separating our sample into low- ($\log(M_\star/\mathrm{M}_\odot) < 10.5$) and high-mass ($\log(M_\star/\mathrm{M}_\odot) > 10.5$) galaxies we found 31 per cent and 52 per cent of our bars are buckled, respectively. This result is in agreement with previous result from Li et al. (2017) and Erwin & Debattista (2017) showing an increase on the fraction of B/P structures with galaxy mass.

We also studied the typical effect that a missing B/P structure would have in our results. We extensively describe the methodology and results of this test in Appendix B. We found that the values of the bar intrinsic semiaxis ratios B/A and C/A would be both systematically overestimated by 0.04 when dismissing the B/P. Similarly, the uncertainties in the intrinsic shape derived by our method (see Table A1) would be underestimated by 0.05 and 0.03 in B/A and C/A, respectively. These small biases could be affecting our galaxies previously classified as hosting a boxy/peanut structure.

The methodology and equations used to derive the intrinsic shape of our bars are extensively discussed in Méndez-Abreu et al. (2010) and Costantin et al. (2018). We refer the readers to those papers for a full description of the problem. Here, we just remind that the scope of our method is to derive, starting from a set of projected geometric parameters for the bar (ellipticity $\epsilon_{\rm bar}$ and position angle $PA_{\rm bar}$) and the disc (ellipticity $\epsilon_{\rm d}$ and position angle $PA_{\rm d}$), the intrinsic semiaxes (A, B, C) of the three-dimensional triaxial ellipsoid describing our bars. The solution to this inversion problem is not unique since we are missing one observable, i.e. the angle subtended by the major axis of the bar and the major axis of the disc in the galaxy plane (Euler ϕ angle). Therefore, our methodology proposes a statistical approach to this problem.

Fig. 3 shows an example of the probability distribution function (PDF) for the intrinsic semiaxis ratios B/A and C/A of some example galaxies in our sample. It is worth noting that the width of the distribution in either B/A and C/A does not only depend on the photometric decomposition errors, but mostly on the lack of knowledge of the Euler ϕ angle. Nevertheless, Fig. 3 shows how our statistical analysis is able to produce important constraints on the shape of our sample bars.

4 RESULTS AND DISCUSSION

4.1 The intrinsic shape of bars in the CALIFA sample

Fig. 4 shows the distribution of the intrinsic axial ratios derived for our sample of bars. The uncertainties in each galaxy are omitted for the sake of clarity in the figure, but they can be found in Table A1. We defined four different regions in this diagram. They represent the expected position for bars with different intrinsic shapes. Following Franx, Illingworth & de Zeeuw (1991) we assume that the three-dimensional galaxy density is structured as a set of coaligned ellipsoids. Therefore, general cases include the oblate-triaxial and prolate-triaxial ellipsoids. Since we do not impose any limitation on the relative size of the ellipsoid semiaxes A, B, and C, they can be defined in-plane (when they are flattened with respect to the disc equatorial plane) and off-plane (when they are elongated along the polar axis). Special cases of this model include the oblate axisymmetric (B=A) and prolate axisymmetric (C=B) spheroids. Then, we classify bars in four categories: oblate-triaxial (or axisymmetric) ellipsoids in-plane ($C/B < B/A$) or off-plane ($C/A > B/C$ and $C/A < 1$), and prolate-triaxial (or axisymmetric) ellipsoids in-plane ($C/A < B/C$ and $C/B > B/A$) or elongated along the polar axis off-plane ($C/A > 1$). Fig. 4 shows the values of the bar intrinsic semiaxis ratios, B/A and C/A, as obtained from the peak of their 2D probability distribution function (yellow star in Fig. 3). However, the final classification for each bar is performed by integrating the 2D PDF of semiaxes ratio within each region of the diagram and finding the region with a higher probability to be occupied by the bar. Different colours in Fig. 4 represent the results of our bar classification. The probabilities for a given bar to have a particular shape are given in Table A1. We found that 68 per cent and 14 per cent of our bars can be classified as prolate-triaxial (or axisymmetric) in-plane and oblate-triaxial (or axisymmetric) in-plane, respectively. Fig. 5 show the distribution of semiaxis ratios B/C and B/A for our sample of prolate-triaxial in-plane and oblate-triaxial in-plane bars, respectively. Prolate-triaxial bars close to $B/C = 1$ can be considered as axisymmetric prolate spheroids whereas oblate-triaxial bars close to $B/A = 1$ can be considered axisymmetric oblate bars. Therefore, our analysis reveals that most of the bars in the nearby Universe are, to first order, prolate-triaxial (or axisymmetric) in the plane of the disc with different degrees of flattening. In addition, we found that bars span a wide range of both $B/A \in [0.1,1]$ and $C/A \in [0.1,0.8]$ values, with median values of $B/A \sim 0.31$ and $C/A \sim 0.34$.

We also found a subclass of oblate-triaxial bars off-plane corresponding to 18 per cent of our sample. It is worth noting that our methodology does not impose a given axial ratio trend such as $A > B > C$, but they are allowed to be free. This particularity of our approach allowed us, for instance, to detect and quantify

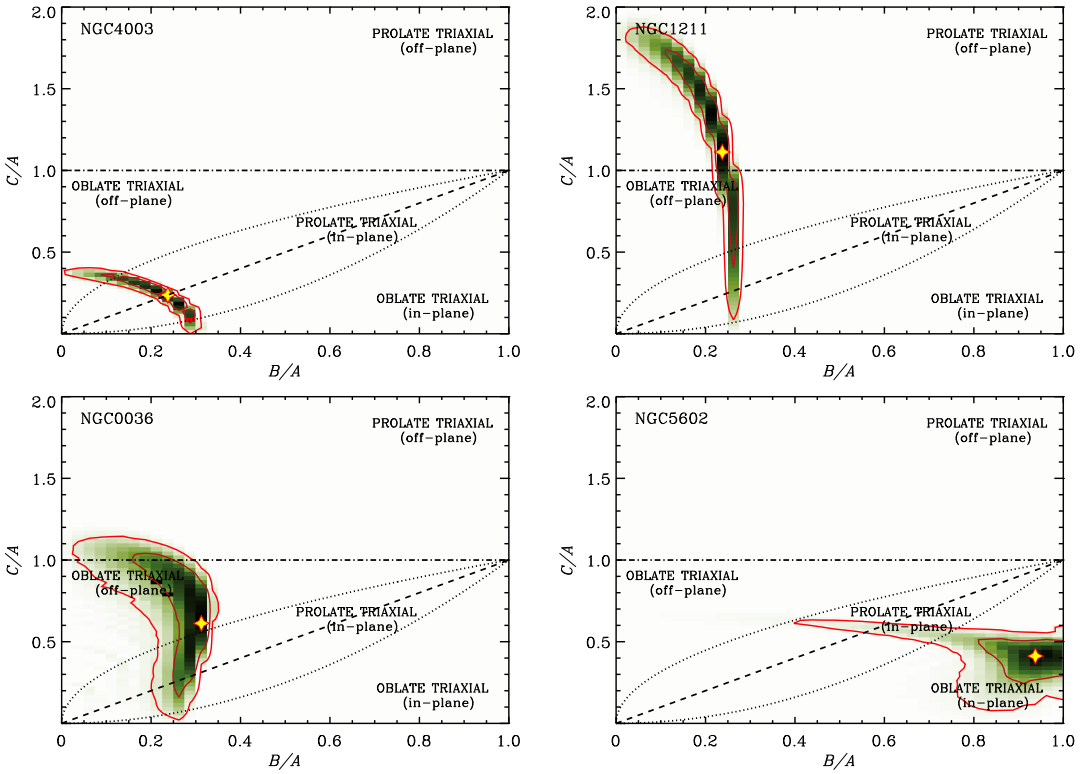

Figure 3. Distribution of the intrinsic axial ratios *B*/*A* and *C*/*A* of four bars in our initial galaxy sample. The yellow star corresponds to the most probable value of *B*/*A* and *C*/*A*. The inner and outer red solid contours represent the 1σ and 2σ probability contours of the intrinsic semiaxes ratios *B*/*A* and *C*/*A* consistent with the bar and disc geometric parameters measured from our photometric decomposition. Different lines mark the regimes of prolate-triaxial (off-plane), prolate-triaxial (in-plane), oblate-triaxial (off-plane), oblate-triaxial (in-plane). We show as an example the four main possible types of bars found in our sample covering the four different shapes. NGC 1211 was removed from the sample due to the large uncertainties in *C*/*A* and it is shown here as an example of prolate-triaxial (off-plane).

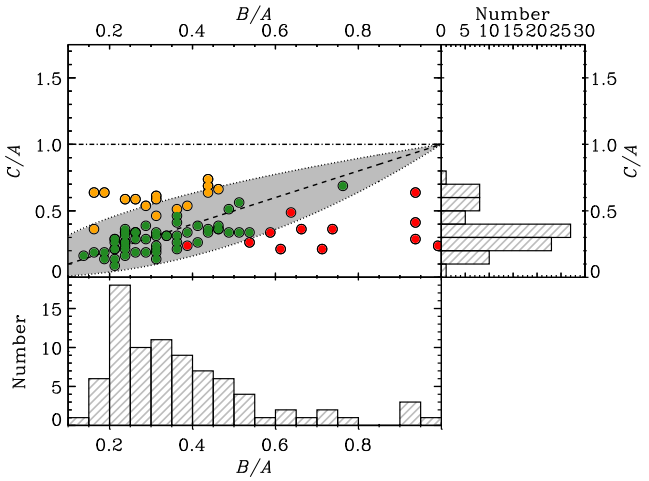

Figure 4. Intrinsic axial ratios our bar sample. Regions are defined as in Fig. 3. Different colours represent bars with intrinsic shapes as derived by integrating their 2D probability distribution function (see text): oblate-triaxial off-plane (orange), oblate-triaxial in-plane (red), and prolate-triaxial in-plane (green). Upper right and lower panels: histograms of the intrinsic *C*/*A* and *B*/*A* axial ratios, respectively.

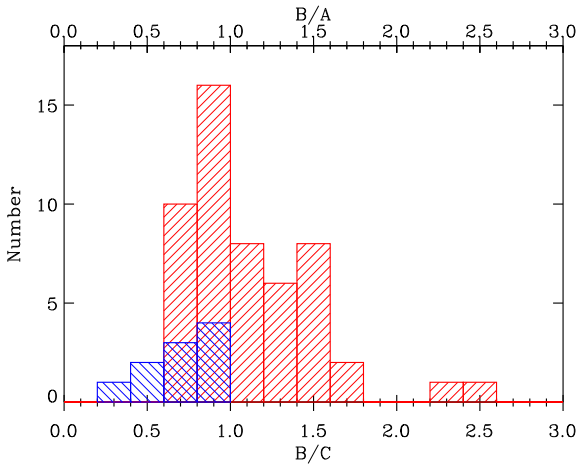

Figure 5. Distribution of intrinsic semiaxis ratios *B*/*C* and *B*/*A* for our sample of prolate-triaxial (red) and oblate-triaxial (blue) bars, respectively. Prolate-triaxial bars close to $B/C = 1$ can be considered prolate axisymmetric bars. Oblate-triaxial bars close to $B/A = 1$ can be considered oblate axisymmetric bars.

the polar bulge of NGC 4698 (Corsini et al. 2012). These galaxies present the largest uncertainties in the *C*/*A* semiaxis among the full sample due to the galaxy/bar orientation with respect to the observer. Therefore, their measurements are also compatible with a less exotic configuration in the galactic plane (see NGC 0036 in Fig. 3 for an example). Other interesting cases in our sample are the four bars with a flattened oblate axisymmetric structure, namely UGC 02134, NGC 4185, NGC 5520, and NGC 5602. We speculate

that these might be examples of lenses that were photometrically fitted as normal bars.

The intrinsic shape of galactic bars has been rarely constrained observationally. Kormendy (1982) suggested that bars are generally triaxial ellipsoids and used an isophotal analysis to estimate their typical semiaxes ratios to be $B/A = 0.2$ and $C/A = 0.1$, with extreme cases such as $B/A < 0.37$ and $0.07 < C/A < 0.25$. Aguerri et al. (2001b) used the photometric approach described in Varela (1992) to derive the intrinsic shape of the bar in NGC 5850. They found a best solution with a triaxial ellipsoid with $0.8 < B/A < 1$ and $0.3 < C/A < 0.4$. More recently, Compère, López-Corredoira & Garzón (2014) used a new 3D photometric decomposition approach to derive the intrinsic shape of a sample of six bars in nearby galaxies. Similarly to us, they found that the C/A semiaxis is more difficult to constrain due to projection problems, and that five out of six bars are compatible with our definition of prolate-triaxial ellipsoids, with the remaining being oblate-triaxial off-plane. They obtain mean values of $B/A = 0.24$ and $C/A = 0.31$ in reasonable good agreement with our findings.

The analysis of the projected, or deprojected, values of the observed bar ellipticity are more common in the literature since they are generally associated with the bar strength (Abraham & Merrifield 2000). Martin (1995) used a 2D deprojection method considering the bar to be infinitesimally thin to derive the deprojected values of the ellipticity. He found that bars cover from $0.2 < b/a < 1$ with a $b/a = 0.49$. A similar result ($b/a = 0.48$) was recently found by Díaz-García et al. (2016) using a sample of barred galaxies from the S4G survey (Sheth et al. 2010) and the deprojection technique developed by Gadotti et al. (2007). Both results show slightly larger values of B/A than those found in this paper. The uncertainties in the derivation of the deprojected values of the bar axis ratio b/a were estimated using mock galaxies in Zou et al. (2014). They found that considering bars as 2D thin ellipsoids, the deprojected ellipticity of the bar can be recovered within a 10 per cent error.

Our analysis of the intrinsic shape of bars suggests that they are generally prolate-triaxial ellipsoids with an intrinsic flattening ($C/A \sim 0.3$), which corresponds to the typical intrinsic flattening of galactic discs at this range of masses (Sánchez-Janssen, Méndez-Abreu & Aguerri 2010; Rodríguez & Padilla 2013). This is in good agreement with the idea that bars form out of disc material, therefore keeping their vertical shape (Sparke & Sellwood 1987). However, numerical simulations have shown how buckling instabilities can quickly change this vertical structure producing a thicker boxy/peanut-shaped component that sticks out of the disc (Combes & Sanders 1981; Pfenniger & Friedli 1991; Debattista et al. 2006). Still, the peanut shape generally does not encompass the full extent of the bar, i.e. there is some flat bar outside the buckled inner part (Lütticke et al. 2000; Athanassoula 2005; Méndez-Abreu et al. 2008; Erwin & Debattista 2013), as has also been claimed for the Milky Way (Martinez-Valpuesta & Gerhard 2011). We discussed extensively the effect of thick B/P structures in the derived shape of our bars in Section 3 and Appendix B. We found that not accounting for the presence of these structures (as it happens in ∼43 per cent of our galaxies) produces the net effect of overestimating B/A and C/A. A rough correction assuming all our galaxies that host a boxy/peanut would produce median values of $B/A \sim 0.27$ and $C/A \sim 0.30$, i.e. still prolate-triaxial ellipsoids with flattening even closer to that of stellar discs.

The results described in this section provide new constraints for future detailed orbital analyses on barred potentials. Historically, 2D analysis used a thin prolate potential to describe the bars (Papayannopoulos & Petrou 1983; Athanassoula et al. 1983; Kaufmann & Patsis 2005; Sellwood & Wilkinson 1993). With the advent of 3D models (somehow promoted by the observational evidence of B/P structures) triaxial potentials with typical axes ratios $B/A = 0.25$ and $C/A = 0.1$, similar to those observationally found by Kormendy (1982), became common (Pfenniger 1984; Skokos et al. 2002; Patsis, Skokos & Athanassoula 2003). However, our results suggest that bars generally have larger values of both B/A and C/A. Using 3D N-body simulations, Pfenniger & Friedli (1991) found that soon after the bar is formed, it has a thin structure with $B/A \sim 0.42$ and $C/A \sim 0.33$, with a later thickening up to $B/A \sim 0.51$ and $C/A \sim 0.40$ when the evolution seems to have ceased. This result is in good agreement with our findings and suggests that some of the orbital analysis potential might be revisited.

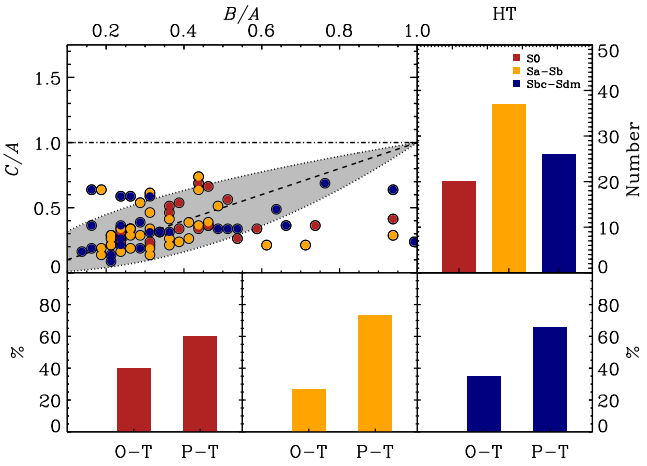

Figure 6. *Top left-hand panel*: Intrinsic axial ratios of our CALIFA sample of bars as a function of the Hubble type (S0s, red symbols; Sa–Sb, yellow symbols; Sbc–Sdm, blue symbols). Different regions represent different intrinsic shapes as in Fig. 3. *Top right-hand panel*: Distribution of Hubble types in our CALIFA sample (S0s: red histogram; Sa–Sb: yellow histogram; Sbc–Sdm: blue histogram). Bottom panels: Distribution of the intrinsic shape of our CALIFA bars (O-T: oblate-triaxial or P-T: prolate-triaxial) as a function of their Hubble type (S0s: red histograms; Sa–Sb: yellow histograms; Sbc–Sdm: blue histograms).

Hydrodynamical simulations have also used triaxial ellipsoids to model the bar potential in 3D. Hunter et al. (1988) found a best model for NGC 3992 with a bar potential with semiaxis ratios $B/A = 0.54$ and $C/A = 0.33$ and England (1989) shows that NGC 1300 can be modelled using a potential with a prolate bar with $B/A = C/A = 0.34$. These results are in agreement with the semiaxis ratios derived for the bars in our sample.

4.2 The relation of the intrinsic shape of bars with galaxy properties

Fig. 6 shows the distribution of the bar intrinsic shapes with the Hubble type of the host galaxies obtained from Walcher et al. (2014). We found a slight trend in the fraction of both oblate-triaxial and prolate-triaxial bars with Hubble type. Oblate-triaxial bars represent 40^{+11}_{-10} per cent, 27^{+8}_{-6} per cent, and 34^{+11}_{-8} per cent of S0, Sa–Sb, and Sbc–Sdm galaxies, respectively. On the other hand, the fraction of prolate-triaxial bars is larger in spirals than S0 galaxies with 60^{+10}_{-11} per cent, 73^{+6}_{-8} per cent, and 66^{+6}_{-8} per cent of the bars in S0, Sa–Sb, and Sbc–Sdm galaxies, respectively. Uncertainties were computed using binomial 68 per cent confidence intervals. Fig. 6 also shows a slight trend towards bars in S0 galaxies having larger values of B/A and C/A than spirals. After discarding the four oblate

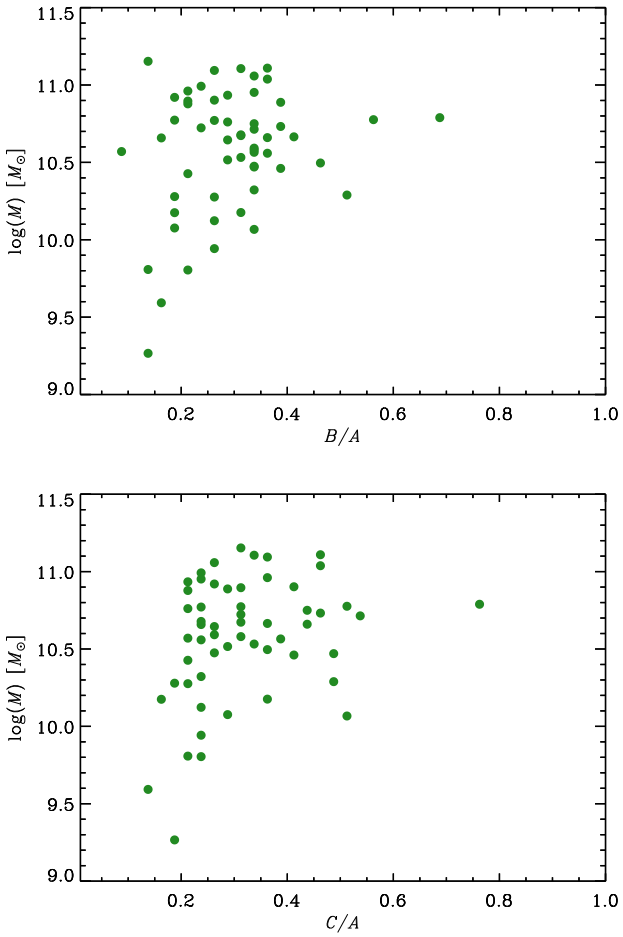

Figure 7. Distribution of the axial ratio *B*/*A* (upper panel) and *C*/*A* (bottom panel) as a function of the galaxy stellar mass for our sample of prolate bars.

axisymmetric bars discussed in the previous section, we found mean values for bars in S0s of $B/A = 0.36 \pm 0.07$ and $C/A = 0.34 \pm 0.07$ whereas for bars in spirals bar we derived $B/A = 0.30 \pm 0.10$ and $C/A = 0.28 \pm 0.08$.

As suggested in the previous section, the flattening of our bars is similar to that expected for discs of similar masses. The dependence of intrinsic semiaxis ratios with the Hubble type is also supportive of this scenario, adding the fact that bars formed in early-type galaxies (S0) or spirals (Sa–Sdm), which statistically have different intrinsic thickening (Ryden 2006), also follow the same trend. This result suggests a strong relation between the flattening of the disc and that of the outer thin bar formed out of it.

Fig. 7 shows the distribution of *B*/*A* and *C*/*A* for our sample of prolate-triaxial bars as a function of the galaxy stellar mass. A trend is present such as bars in less massive galaxies are intrinsically more flattened (less *C*/*A*) and more elliptical (less *B*/*A*) than in high-mass systems. In fact, it seems that high-mass galaxies ($\langle \log(M_\star/\mathrm{M}_\odot) \rangle > 10.5$) can have large values of both *B*/*A* and *C*/*A* whereas low-mass galaxies ($\langle \log(M_\star/\mathrm{M}_\odot) \rangle < 10.5$) are confined to low values of *B*/*A* and *C*/*A*. The Spearman correlation coefficients and *p*-values are $\rho = 0.3$ ($p = 0.02$) and $\rho = 0.2$ ($p = 0.2$) for *B*/*A* and *C*/*A*, respectively. Thus, the correlation with *C*/*A* cannot be considered as statistically significative. In Méndez-Abreu et al. (2017), we discussed the relation between Hubble type and galaxy mass for the CALIFA sample, with later types being systematically less massive galaxies. We found a similar, but less strong trend for our limited sample of 83 barred galaxies (S0 $\langle \log(M_\star/\mathrm{M}_\odot) \rangle = 10.7 \pm 0.2$; Sa–Sb $\log(M_\star/\mathrm{M}_\odot) = 10.6 \pm 0.3$; Sbc–Sdm $log(M_\star/\mathrm{M}_\odot) = 10.1 \pm 0.6$). Table1 shows the mean values of the intrinsic flattening of our sample of prolate bars with both stellar mass and Hubble type. The relation with the Hubble type is still present for the low-mass bin, but it is not clear for the high-mass one. However, the low number statistics makes it difficult to extract further conclusions on whether it is the mass or the Hubble type driving our correlations.

Table 1. Mean values of the intrinsic semiaxes ratios *B*/*A* and *C*/*A* of our sample of prolate bars as a function of mass and Hubble type.

	S0	Sa–Sb	Sbc–Sdm
$\log(M_\star/\mathrm{M}_\odot) < 10.5$; *B*/*A*	0.31 ± 0.07	0.28 ± 0.12	0.29 ± 0.13
$\log(M_\star/\mathrm{M}_\odot) < 10.5$; *C*/*A*	0.40 ± 0.09	0.29 ± 0.13	0.24 ± 0.07
$\log(M_\star/\mathrm{M}_\odot) > 10.5$; *B*/*A*	0.37 ± 0.10	0.30 ± 0.08	0.38 ± 0.20
$\log(M_\star/\mathrm{M}_\odot) > 10.5$; *C*/*A*	0.33 ± 0.10	0.28 ± 0.08	0.36 ± 0.18

We also look for correlations between the intrinsic shape of our prolate-triaxial bars with the properties of the individual structures shaping our galaxies, i.e. bulges, discs, and the bars themselves. Fig. 8 shows the most significant trends. Regarding the bulge properties, we found that either *B*/*A* and *C*/*A* correlates with the Sérsic index and *B*/*T* ratio. The relation is stronger with the *B*/*T* ratio (Fig. 8), where we found a Spearman correlation coefficient $\rho = 0.35$ ($p = 0.009$) and $\rho = 0.41$ ($p = 0.002$) for *B*/*A* and *C*/*A*, respectively. These correlations indicate that more prominent (larger *B*/*T*) and more concentrated (larger n) bulges are related with thicker (larger *C*/*A*) and more circular bars (larger *B*/*A*). Despite the fact that we did not find any correlation with the effective radii of the bulges (r_e), we did find a strong correlation when normalized by the bar radius ($r_\mathrm{e}/r_\mathrm{bar}$). Our analysis shows $\rho = 0.47$ ($p = 0.0004$) and $\rho = 0.52$ ($p = 8\mathrm{e}{-5}$) for the relation between $r_\mathrm{e}/r_\mathrm{bar}$ vs. *B*/*A* and *C*/*A*, respectively (see Fig. 8). Regarding disc parameters, we only found a weak correlation of the bars intrinsic shape with the $g - r$ colour of the disc. Fig. 8 shows these results where we find a Spearman coefficient of $\rho = 0.34$ ($p = 0.02$) and $\rho = 0.25$ (p=0.08) for *B*/*A* and *C*/*A*, respectively. Therefore, redder discs have thicker and more circular bars (but notice that the relation with *C*/*A* is not statistically significant). Finally, we explored the photometric properties of the bars. We found that *C*/*A* correlates with all bar parameters: $\mu_{0,\,\mathrm{bar}}$ ($\rho = -0.46$, $p = 0.0003$), r_bar ($\rho = -0.33$, $p = 0.01$), and *Bar*/*T* ratio ($\rho = -0.32$, $p = 0.02$). On the other hand, *B*/*A* did not correlate with any bar parameter. These relations point towards more prominent (larger *Bar*/*T*), brighter (larger $\mu_{0,\,\mathrm{bar}}$), and shorter (smaller r_bar) bars being thicker (larger *C*/*A*).

The presence of correlations between the intrinsic shape of the bars and the properties of the different structures composing disc galaxies is not surprising since bars are formed by internal secular mechanisms out of disc material (Hohl 1971; Kalnajs 1972; Athanassoula & Misiriotis 2002), and their evolution is strongly related to the bulge–disc–halo interaction (Debattista & Sellwood 2000; Weinberg & Katz 2007; Athanassoula et al. 2013; Long, Shlosman & Heller 2014). Some observational studies found that bulges influence the size, strength, and incidence of bars (Aguerri et al. 2009; Laurikainen et al. 2009; Cheung et al. 2013), since bulges contribute significantly to the radial force in discs, bulge masses, and sizes can affect bar formation (Hohl 1976; Efstathiou, Lake & Negroponte 1982). However, most of these earlier studies considered the spheroidal component as a halo, not as a bulge, and more recent studies focus mainly in the formation of the bar and not in their properties (Scannapieco & Athanassoula 2012; Kataria &

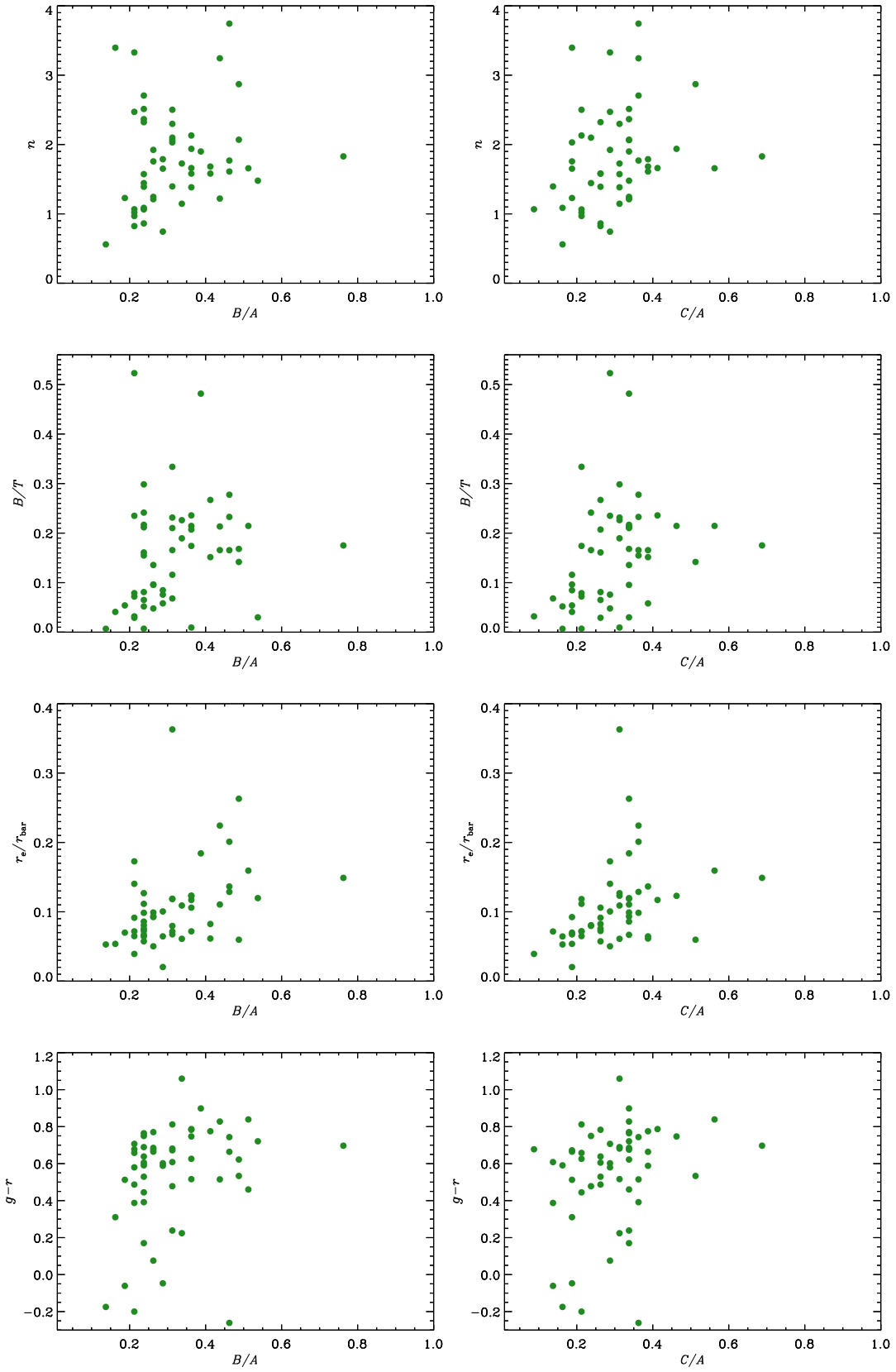

Figure 8. Distribution of the intrinsic axis ratios *B*/*A* (left-hamd panels) and *C*/*A* (right-hand panels) for our sample of prolate bars as a function of (from top to bottom) bulge Sérsic index (n), bulge-to-total luminosity ratio (B/T), the bulge effective radius over bar radius ratio (r_e/r_{bar}), and the colour of the disc ($g - r$).

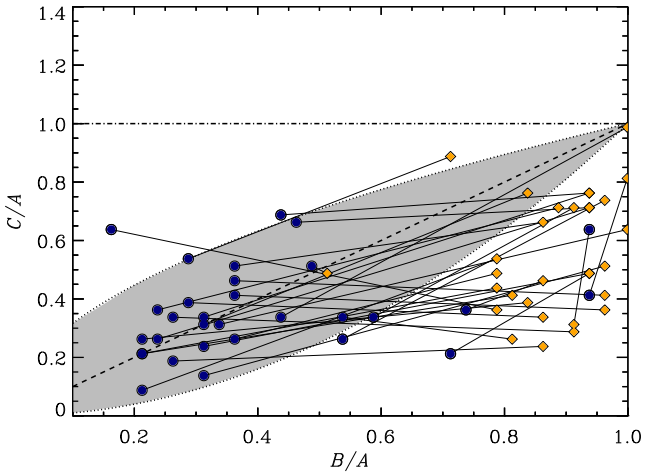

Figure 9. Intrinsic axial ratios of our CALIFA sample of bars (blue circles) and bulges (yellow diamonds). Structures belonging to the same galaxy are linked by a solid line.

Das 2018). Therefore, more numerical simulations focused on the bar properties are needed to understand the dependence of the bar intrinsic shape with the bulge properties that we find in this paper.

4.3 Bars vs bulges: the connection with bulge growth

In Costantin et al. (2018), we derived the intrinsic shape of the bulges present in the CALIFA sample of galaxies. We followed a similar methodology as the one used in this paper and we found that, contrary to galactic bars, bulges tend to be nearly oblate systems (66 per cent), with a smaller fraction of prolate spheroids (19 per cent) and triaxial ellipsoids (15 per cent). We also found that those bulges sharing potential with a galactic bar represented the majority of our triaxial bulges (75 per cent). Fig. 9 shows the relation between the intrinsic axial ratios of both bars and bulges for the 31 galaxies in common with Costantin et al. (2018). We can distinguish two main behaviours in this diagram: i) bulges that are thicker than their surrounding bars and ii) bulges that are thinner than the surrounding bar. We computed the differences between the intrinsic flattening of both bulges and bars using the marginal *C*/*A* distribution obtained from the PDF for each structure. Since both distributions are independent, for each galaxy we randomly sampled the *C*/*A* PDF of the bar and bulge (see Fig. 3 for examples) and computed for every pair of values whether the bulge has a larger or smaller *C*/*A* than the bar. We derived that 52 per cent and 13 per cent of our bulges are more vertically prominent than their surrounding bars at 1σ and 3σ levels, respectively. Similarly, we found that 16 per cent of our bulges are more flattened that their bars at 1σ level. In general, those bulges with *C*/*A* and *B*/*A* close to 1, i.e. with a nearly spherical shape, are surrounded by a prolate thinner bar. On the other hand, oblate-triaxial (or axisimmetric) bulges which are flattened in the vertical direction have an intrinsic flattening similar to that of the bar.

The intrinsic shape of bulges has been proposed as a way to distinguish between bulges formed at early stages of the Universe by dissipative processes (classical bulges; Athanassoula 2005; Brooks & Christensen 2016) and those formed by secular processes within the galaxy (disc-like bulges Kormendy & Kennicutt 2004). Recent works by Costantin et al. (2018) and Costantin et al. (in prep.) have shown that oblate-triaxial bulges which are intrinsically flattened in-plane might be considered as disc-like bulges whereas oblate-triaxial non-flattened bulges show properties of classical bulges. The main internal mechanism to form a disc-like bulge is gas flowing inwards to the galaxy centre thanks to the torque exerted by a bar structure (Pfenniger & Norman 1990; Friedli & Benz 1995). This gas then accumulates in the centre forming a new rotationally-supported bulge (Kormendy & Kennicutt 2004; Boone et al. 2007; Wozniak & Michel-Dansac 2009). We have demonstrated how the intrinsic flattening of the majority of our long bars is strongly related to vertical extension of the host disc, therefore, the results shown in Fig. 9, with 16 per cent of the bulges having lower intrinsic flattening than the corresponding bar (and also similar to the disc) make these bulges the perfect candidates to be disc-like bulges. On the other hand, spherical bulges hosted within thinner bars (and thinner discs) might have been created by different (not internal secular) processes and therefore they could represent a population of classical bulges. The presence of classical bulges, and their coexistence with both disc-like bulges and boxy/peanuts structures, in barred galaxies has been studied in the literature (de Lorenzo-Cáceres et al. 2012; Méndez-Abreu et al. 2014; Erwin et al. 2015). However, their identification generally requires the use of photometric and spectroscopic information. The results of this paper reinforce the idea that the intrinsic shape of bulges provides key information on their classification, specially in barred galaxies where it can be directly compared with that of the bar (similar to that of the disc). Furthermore, the 3D structure of the bulge is derived using only photometric information so it could be applied to larger samples of galaxies.

5 CONCLUSIONS

We present the first statistical study on the 3D intrinsic shape of galactic bars in the nearby Universe. We analysed a sample of 83 barred galaxies extracted from the CALIFA-DR3 survey with the galaXYZ code (Méndez-Abreu et al. 2010; Costantin et al. 2018). This method is purely based on photometric information and uses the projected geometric parameters (ellipticities and position angles) of both bars and discs obtained from a careful multicomponent photometric decomposition (Méndez-Abreu et al. 2017).

Our analysis consider galactic bars as single triaxial ellipsoidal structures. We discuss that our results are representative of the outer thin bar due to the way photometric decompositions of the galaxies were performed. Using mock galaxy simulations, we derive that the possible presence of a vertically thick component in the bar inner regions (boxy/peanut structure) would produce an overestimation of 0.04 in both *B*/*A* and *C*/*A* intrinsic semiaxes. Our main results on the intrinsic shape of outer thin bars are:

(i) Bars are mainly prolate-triaxial (or axisymmetric) in-plane ellipsoids (67 per cent), with another 14 per cent of bars characterized as oblate-triaxial (or axisymmetric) in-plane ellipsoids. They have a typical intrinsic flattening C/A = 0.34, which matches the intrinsic flattening of galactic discs of similar stellar masses (Sánchez-Janssen et al. 2010).

(ii) The intrinsic flattening of our prolate-triaxial bars is dependent on the galaxy Hubble type and galaxy stellar mass. In our sample, the Hubble type is related to the galaxy mass, but due to low number statistics it is difficult to separate which galaxy property is driving the vertical growth of the outer bar. We also found correlations of the bar flattening with bulge (n, B/T), disc (colour $g-r$), and bar ($\mu_{0,\,bar}$, $r_{\rm bar}$, Bar/T) properties, suggesting that bar evolution is tightly related with the structures of the host galaxy.

(iii) We compared the relative flattening of bars and bulges for a subsample of 31 galaxies in common with the sample of Costantin et al. (2018). We found that 52 per cent and 16 per cent of bulges are either more or less vertically extended than their surrounding bar at 1 sigma level, respectively. Assuming that (as we demonstrate in this paper) the intrinsic flattening of bars and discs are similar, we suggest that these percentages might be representative of the fraction of classical and disc-like bulges in our sample.

This paper represents our first attempt to extend our methodology to derive the intrinsic shape of galactic structure in individual galaxies beyond the properties of bulges. The study of the evolution of the intrinsic shape of bars contains important information about both the evolution of these systems and the creation of inner structures, since the axis ratio of the bar has been recognized as an important quantity which drives, for instance, the amount of gas that is driven to the galaxy centre by the bar torques (Friedli & Benz 1993). Further studies on the evolution of the intrinsic shape of bars with both cosmic time and dynamical properties of the galaxies will be presented in forthcoming papers, providing further constraints for numerical simulations.

ACKNOWLEDGEMENTS

We thank the anonymous referee for her/his many valuable comments which helped to improve this paper. JMA and JALA acknowledge support from the Spanish Ministerio de Economia y Competitividad (MINECO) by the grant AYA2013-43188-P. AdLC acknowledges support from the Spanish Ministerio de Economia y Competitividad (MINECO) grant AYA2011-24728. EMC is supported by Padua University through grants 60A02-5857/13, 60A02-5833/14, 60A02-4434/15, and CPDA133894. This paper is based on data from the Calar Alto Legacy Integral Field Area Survey, CALIFA (http://califa.caha.es), funded by the Spanish Ministery of Science under grant ICTS-2009-10, and the Centro Astronómico Hispano-Alemán.

Based on observations collected at the Centro Astronómico Hispano Alemán (CAHA) at Calar Alto, operated jointly by the Max-Planck Institut für Astronomie and the Instituto de Astrofísica de Andalucía (CSIC).

REFERENCES

Abraham R. G., Merrifield M. R., 2000, AJ, 120, 2835
Aguerri J. A. L., Balcells M., Peletier R. F., 2001a, A&A, 367, 428
Aguerri J. A. L., Hunter J. H., Prieto M., Varela A. M., Gottesman S. T., Muñoz-Tuñón C., 2001b, A&A, 373, 786
Aguerri J. A. L., Méndez-Abreu J., Corsini E. M., 2009, A&A, 495, 491
Athanassoula E., 1992, MNRAS, 259, 328
Athanassoula E., 2003, MNRAS, 341, 1179
Athanassoula E., 2005, MNRAS, 358, 1477
Athanassoula E., Misiriotis A., 2002, MNRAS, 330, 35
Athanassoula E., Bienayme O., Martinet L., Pfenniger D., 1983, A&A, 127, 349
Athanassoula E., Machado R. E. G., Rodionov S. A., 2013, MNRAS, 429, 1949
Athanassoula E., Laurikainen E., Salo H., Bosma A., 2015, MNRAS, 454, 3843
Barazza F. D. et al., 2009, A&A, 497, 713
Barazza F. D., Jogee S., Marinova I., 2008, ApJ, 675, 1194
Boone F. et al., 2007, A&A, 471, 113
Brooks A., Christensen C., 2016, Galactic Bulges, 418, 317
Buta R. J., Byrd G. G., Freeman T., 2003, AJ, 125, 634
Cheung E. et al., 2013, ApJ, 779, 162
Ciambur B. C., Graham A. W., 2016, MNRAS, 459, 1276
Combes F., Sanders R. H., 1981, A&A, 96, 164
Combes F., Debbasch F., Friedli D., Pfenniger D., 1990, A&A, 233, 82
Compère P., López-Corredoira M., Garzón F., 2014, A&A, 571, A98
Consolandi G., 2016, A&A, 595, A67
Contopoulos G., Papayannopoulos T., 1980, A&A, 92, 33
Corsini E. M., Méndez-Abreu J., Pastorello N., Dalla Bontà E., Morelli L., Beifiori A., Pizzella A., Bertola F., 2012, MNRAS, 423, L79
Costantin L., Méndez-Abreu J., Corsini E. M., Eliche-Moral M. C., Tapia T., Morelli L., Dalla Bontà E., Pizzella A., 2018, A&A, 609, A132
de Lorenzo-Cáceres A., Vazdekis A., Aguerri J. A. L., Corsini E. M., Debattista V. P., 2012, MNRAS, 420, 1092
de Lorenzo-Cáceres A., Falcón-Barroso J., Vazdekis A., 2013, MNRAS, 431, 2397
Debattista V. P., Sellwood J. A., 1998, ApJ, 493, L5
Debattista V. P., Sellwood J. A., 2000, ApJ, 543, 704
Debattista V. P., Shen J., 2007, ApJ, 654, L127
Debattista V. P., Mayer L., Carollo C. M., Moore B., Wadsley J., Quinn T., 2006, ApJ, 645, 209
Díaz-García S., Salo H., Laurikainen E., Herrera-Endoqui M., 2016, A&A, 587, A160
Efstathiou G., Lake G., Negroponte J., 1982, MNRAS, 199, 1069
England M. N., 1989, ApJ, 344, 669
Erwin P. et al., 2015, MNRAS, 446, 4039
Erwin P., 2004, A&A, 415, 941
Erwin P., 2018, MNRAS, 474, 5372
Erwin P., Debattista V. P., 2013, MNRAS, 431, 3060
Erwin P., Debattista V. P., 2017, MNRAS, 468, 2058
Franx M., Illingworth G., de Zeeuw T., 1991, ApJ, 383, 112
Friedli D., Benz W., 1993, A&A, 268, 65
Friedli D., Benz W., 1995, A&A, 301, 649
Gadotti D. A., Athanassoula E., Carrasco L., Bosma A., de Souza R. E., Recillas E., 2007, MNRAS, 381, 943
Hohl F., 1971, ApJ, 168, 343
Hohl F., 1976, AJ, 81, 30
Hunter J. H., Jr., England M. N., Gottesman S. T., Ball R., Huntley J. M., 1988, ApJ, 324, 721
Kalnajs A. J., 1972, ApJ, 175, 63
Kataria S. K., Das M., 2018, MNRAS, 475, 1653
Kaufmann D. E., Patsis P. A., 2005, ApJ, 624, 693
Kormendy J., 1982, Morphology and dynamics of galaxies; Proceedings of the Twelfth Advanced Course, Saas-Fee, Switzerland, March 29-April 3, 1982 (A84-15502 04-90). Sauverny, Switzerland, Observatoire de Geneve, 1983, p. 113–288., 12, 113
Kormendy J., Kennicutt R. C., Jr., 2004, ARA&A, 42, 603
Kruk S. J. et al., 2017, MNRAS, 469, 3363
Laurikainen E., Salo H., 2016, in Laurikainen E., Peletier R., Gadotti D., eds, Astrophysics and Space Science Library Vol. 418, Galactic Bulges. p. 77
Laurikainen E., Salo H., 2017, A&A, 598, A10
Laurikainen E., Salo H., Buta R., Knapen J. H., 2009, ApJ, 692, L34
Laurikainen E., Salo H., Buta R., Knapen J. H., 2011, MNRAS, 418, 1452
Laurikainen E., Salo H., Athanassoula E., Bosma A., Buta R., Janz J., 2013, MNRAS, 430, 3489
Li Z.-Y., Ho L. C., Barth A. J., 2017, ApJ, 845, 87
Long S., Shlosman I., Heller C., 2014, ApJ, 783, L18
Lütticke R., Dettmar R.-J., Pohlen M., 2000, A&AS, 145, 405
Marinova I., Jogee S., 2007, ApJ, 659, 1176
Martin P., 1995, AJ, 109, 2428
Martinez-Valpuesta I., Gerhard O., 2011, ApJ, 734, L20
Martinez-Valpuesta I., Shlosman I., Heller C., 2006, ApJ, 637, 214
Martinez-Valpuesta I., Aguerri J. A. L., González-García A. C., Dalla Vecchia C., Stringer M., 2017, MNRAS, 464, 1502
Masters K. L. et al., 2011, MNRAS, 411, 2026
Méndez-Abreu J. et al., 2017, A&A, 598, A32
Méndez-Abreu J., Corsini E. M., Debattista V. P., De Rijcke S., Aguerri J. A. L., Pizzella A., 2008, ApJ, 679, L73

Méndez-Abreu J., Simonneau E., Aguerri J. A. L., Corsini E. M., 2010, A&A, 521, A71+
Méndez-Abreu J., Sánchez-Janssen R., Aguerri J. A. L., Corsini E. M., Zarattini S., 2012, ApJ, 761, L6
Méndez-Abreu J., Debattista V. P., Corsini E. M., Aguerri J. A. L., 2014, A&A, 572, A25
Muñoz-Tuñón C., Caon N., Aguerri J. A. L., 2004, AJ, 127, 58
Nair P. B., Abraham R. G., 2010, ApJ, 714, L260
Papayannopoulos T., Petrou M., 1983, A&A, 119, 21
Patsis P. A., Skokos C., Athanassoula E., 2003, MNRAS, 342, 69
Pfenniger D., 1984, A&A, 134, 373
Pfenniger D., Friedli D., 1991, A&A, 252, 75
Pfenniger D., Norman C., 1990, ApJ, 363, 391
Raha N., Sellwood J. A., James R. A., Kahn F. D., 1991, Nature, 352, 411
Rodríguez S., Padilla N. D., 2013, MNRAS, 434, 2153
Ryden B. S., 2006, ApJ, 641, 773
Sánchez S. F. et al., 2016, A&A, 594, A36
Sánchez-Janssen R., Méndez-Abreu J., Aguerri J. A. L., 2010, MNRAS, 406, L65
Scannapieco C., Athanassoula E., 2012, MNRAS, 425, L10
Sellwood J. A., Debattista V. P., 2006, ApJ, 639, 868
Sellwood J. A., Wilkinson A., 1993, Reports on Progress in Physics, 56, 173
Sheth K. et al., 2010, PASP, 122, 1397
Sheth K., Vogel S. N., Regan M. W., Thornley M. D., Teuben P. J., 2005, ApJ, 632, 217
Shlosman I., Begelman M. C., Frank J., 1990, Nature, 345, 679
Skibba R. A. et al., 2012, MNRAS, 423, 1485
Skokos C., Patsis P. A., Athanassoula E., 2002, MNRAS, 333, 847
Sparke L. S., Sellwood J. A., 1987, MNRAS, 225, 653
Varela A. M., 1992, PhD thesis, PhD thesis, Instituto de Astrofísica de Canarias, (1992)
Walcher C. J. et al., 2014, A&A, 569, A1
Weinberg M. D., Katz N., 2007, MNRAS, 375, 425
Wozniak H., Michel-Dansac L., 2009, A&A, 494, 11
Yoshino A., Yamauchi C., 2015, MNRAS, 446, 3749
Zou Y., Shen J., Li Z.-Y., 2014, ApJ, 791, 11

APPENDIX A: STRUCTURAL PARAMETERS OF THE GALAXY SAMPLE

APPENDIX B: INFLUENCE OF BOXY/PEANUT STRUCTURES IN THE PHOTOMETRIC DECOMPOSITION OF BARS

We devised a set of galaxy image simulations to derive the influence of a boxy/peanut inner component in the geometric parameters of the bars obtained from our photometric decomposition. To this aim, we used a similar approach to that described in Section 5.2 of Méndez-Abreu et al. (2017). We generated 500 mock galaxies comprsed by a bulge (described using a Sérsic distribution), a disc (exponential), an outer bar (Ferrers), and an inner boxy/peanut structure modelled with another Ferrers profile. We considered the inner boxy/peanut structure to be the same structure as the barlenses described in Laurikainen et al. (2011, 2013). The use of either a Ferrers or Sérsic profile to describe the barlens surface brigthness distribution was mentioned by Athanassoula et al. (2015) as giving similar results. We opted for a Ferrers profile since it was more directly comparable with the available observational constraints for barlenses, in particular to create a model with given ratios between the length of the outer and inner regions of the bar. The range of values used to build the bulge, disc, and bar components were taken from Méndez-Abreu et al. (2017), including $q_{\rm disk}$= [0.55,1] and $q_{\rm bar}$ = [0.2, 0.4]. They are representative of the structural parameters in the i −band for barred galaxies present in the CALIFA survey. The values of the Ferrers profile used to describe the barlens structure were extracted from Athanassoula et al. (2015) and Laurikainen & Salo (2017). We used random values between the following ranges: $L_{\rm bl}/L_{\rm bar}$ = [0.31, 1.3], $r_{\rm bl}/r_{\rm bar}$ = [0.4, 0.8], $q_{\rm bl}$ = [0.5, 1], $\rm PA_{bl}$=$\rm PA_{bar}$.

The mock galaxies were analysed as if they were pure barred galaxies without any inner boxy/peanut component, i.e. only a bulge, a disc, and the outer parts of the bar were considered to model the galaxy light. This allowed us to quantify the effect of the boxy/peanut surface brightness distribution on the photometric decomposition of our barred galaxies, in particular, the effect of the ellipticities and position angles. Fig. B1 shows the differences in the four structural parameters involved in our analysis ($q_{\rm bar}$, $q_{\rm disc}$, $\rm PA_{bar}$, $\rm PA_{disc}$) due to the addition of a barlens structure in the galaxy centre. We compute the mean (systematic) and rms (statistical) errors between the input and output values of the mock galaxies obtaining that: $q_{\rm bar}$(in) − $q_{\rm bar}$ (out) = −0.037 ± 0.048, $q_{\rm disc}$(in) − $q_{\rm disc}$(out) = −0.007 ± 0.031 , $\rm PA_{bar}$ (in) − $\rm PA_{bar}$ (out) = −0.03 ± 0.51, $\rm PA_{disc}$ (in) − $\rm PA_{disc}$ (out) = 0.14 ± 2.25. Despite the fact that the statistical errors are always larger than any possible systematic, we found a weak bias of the bar axis ratio towards larger values when including the barlens component. This can be expected if part of the barlens surface brightness, which is always rounder than the outer bar, is incoporated into the bar component.

At this point, we study how the previous errors in the observational measurements propagate into the derived intrinsic shape of bulges. We used both the systematic and statistical errors to understand their effect into the intrinsic *B*/*A* and *C*/*A* semiaxis ratios. First, we recomputed the bar intrinsic shape (using the methodology described in Section 3) correcting for the mean deviations (systematic) in the observational parameters obtained previosuly. This will provide us with the typical difference in the *B*/*A* and *C*/*A* values assuming that all galaxies host a barlens structure. Second, we recomputed the typical uncertainty in the bar intrinsic shape by assuming the photometric errors in the observational parameters to be the statistical errors computed using the barlens simulations. This help us to quantify how the uncertainties in the intrinsic *B*/*A* and *C*/*A* semiaxes are affected by the presence of a barlens structure. Fig. B2 show the results of this analysis. We found that, if a galaxy have a barlens structure that has not been included in the photometric decomposition procedure, both *B*/*A* and *C*/*A* would be systematically overestimated by 0.04 and 0.04, respectively. Similarly, the uncertainties in the intrinsic shape derived by our method (Section 3) would be understimated by 0.05 and 0.03 in *B*/*A* and *C*/*A*, respectively. Therefore, even if the results presented in this paper are not affected by the possible presence of an inner boxy/peanut structure (characterized here as a barlens), small variations can be found.

Table A1. Main properties and structural parameters of our CALIFA sample of galaxies.

Galaxy	Redshift	$\log(M_\star/M_\odot)$	HT	$g-r$ (disc)	μ_0	n	r_e	q_d	q_{bar}	PA_d	PA_{bar}	B/A	C/A	P(pro. o)	P(pro. i)	P(obl. o)	P(obl. i)	V. class
(1)	(2)	(3)	(4)	(5)	(6)	(7)	(8)	(9)	(10)	(11)	(12)	(13)	(14)	(15)	(16)	(17)	(18)	(19)
UGC00036	0.0206	10.764	Sab	0.78	19.1	1.52	0.54	0.47 ± 0.01	0.668 ± 0.007	17.9 ± 0.7	133.3 ± 0.4	$0.44^{0.46}_{0.26}$	$0.64^{0.96}_{0.21}$	0.01	0.44	0.55	0.00	Barlens?
NGC 0036	0.0197	10.746	Sb	0.69	20.2	4.93	2.46	0.57 ± 0.01	0.465 ± 0.007	16.7 ± 0.7	124.1 ± 0.4	$0.31^{0.31}_{0.16}$	$0.62^{1.04}_{0.16}$	0.07	0.26	0.66	0.01	Barlens
NGC 0165	0.0192	10.482	Sb	0.60	20.3	0.74	0.78	0.81 ± 0.01	0.295 ± 0.007	83.3 ± 0.7	62.6 ± 0.4	$0.29^{0.34}_{0.14}$	$0.29^{0.46}_{0.11}$	0.00	0.66	0.27	0.07	Barlens?
NGC 0180	0.0172	10.597	Sb	0.59	20.2	1.09	0.67	0.682 ± 0.007	0.227 ± 0.006	165.8 ± 0.3	141.9 ± 0.2	$0.24^{0.26}_{0.14}$	$0.16^{0.26}_{0.09}$	0.00	0.82	0.10	0.08	Barlens
NGC 0214	0.0148	10.467	Sbc	0.60	19.0	1.10	0.56	0.705 ± 0.007	0.564 ± 0.006	57.4 ± 0.3	60.1 ± 0.2	$0.64^{0.84}_{0.39}$	$0.49^{0.69}_{0.09}$	0.00	0.27	0.09	0.64	None
NGC 0364	0.0166	10.647	E7	0.83	19.9	1.55	0.58	0.73 ± 0.01	0.548 ± 0.007	33.3 ± 0.7	91.9 ± 0.4	$0.44^{0.46}_{0.24}$	$0.69^{1.11}_{0.16}$	0.19	0.32	0.46	0.03	Barlens
NGC 0447	0.0183	10.901	Sa	0.76	21.2	2.37	1.25	0.858 ± 0.007	0.270 ± 0.006	28.2 ± 0.3	17.5 ± 0.2	$0.24^{0.31}_{0.12}$	$0.34^{0.49}_{0.11}$	0.00	0.66	0.30	0.04	Barlens
IC1683	0.0159	10.461	Sb	0.72	20.8	1.68	0.53	0.59 ± 0.01	0.509 ± 0.007	13.5 ± 0.7	157.0 ± 0.4	$0.41^{0.46}_{0.21}$	$0.39^{0.59}_{0.11}$	0.00	0.66	0.22	0.12	None
NGC 0551	0.0170	10.528	Sbc	0.68	19.5	1.07	0.43	0.44 ± 0.01	0.194 ± 0.007	135.9 ± 0.7	160.2 ± 0.4	$0.21^{0.24}_{0.09}$	$0.09^{0.16}_{0.04}$	0.00	0.83	0.02	0.15	None
NGC 0570	0.0178	10.879	Sb	0.75	20.4	1.86	1.00	0.90 ± 0.01	0.335 ± 0.007	138.0 ± 0.7	94.0 ± 0.4	$0.29^{0.34}_{0.14}$	$0.54^{0.94}_{0.19}$	0.02	0.29	0.68	0.02	Barlens
UGC01271	0.0164	10.532	S0a	1.06	20.0	1.73	0.68	0.63 ± 0.01	0.427 ± 0.007	93.9 ± 0.7	52.1 ± 0.4	$0.34^{0.36}_{0.14}$	$0.31^{0.54}_{0.11}$	0.00	0.68	0.26	0.06	Barlens
NGC 0716	0.0147	10.555	Sb	0.69	18.9	–	–	0.48 ± 0.01	0.469 ± 0.006	62 ± 1.0	13.2 ± 0.5	$0.26^{0.29}_{0.11}$	$0.34^{0.49}_{0.11}$	0.00	0.75	0.22	0.03	None
NGC 0776	0.0159	10.597	Sb	0.74	20.3	1.36	0.59	0.90 ± 0.01	0.349 ± 0.007	146.4 ± 0.7	130.9 ± 0.4	$0.31^{0.36}_{0.14}$	$0.46^{0.76}_{0.19}$	0.00	0.43	0.53	0.04	None
NGC 0842	0.0124	10.460	S0	0.73	19.8	2.60	0.57	0.525 ± 0.004	0.540 ± 0.003	145.1 ± 0.3	155.6 ± 0.2	$0.74^{0.79}_{0.46}$	$0.36^{0.54}_{0.14}$	0.00	0.28	0.04	0.68	None
UGC01918	0.0165	10.551	Sb	0.76	20.2	1.14	0.31	0.45 ± 0.01	0.62 ± 0.02	117.3 ± 0.9	13.7 ± 0.8	$0.44^{0.51}_{0.26}$	$0.74^{1.20}_{0.24}$	0.27	0.25	0.48	0.00	None
NGC 0976	0.0139	10.774	Sbc	0.70	19.1	1.83	0.77	0.786 ± 0.007	0.777 ± 0.006	159.6 ± 0.3	10.6 ± 0.2	$0.76^{0.79}_{0.59}$	$0.69^{1.06}_{0.24}$	0.19	0.31	0.18	0.31	None
UGC02134	0.0149	10.479	Sb	0.74	19.7	2.61	0.93	0.441 ± 0.009	0.470 ± 0.007	105.5 ± 0.5	103.9 ± 0.4	$0.94^{0.96}_{0.86}$	$0.29^{0.41}_{0.16}$	0.00	0.04	0.00	0.96	BP?
NGC 1093	0.0172	10.392	Sbc	0.62	20.0	2.07	1.70	0.67 ± 0.01	0.448 ± 0.007	96.5 ± 0.7	116.5 ± 0.4	$0.49^{0.56}_{0.29}$	$0.34^{0.51}_{0.09}$	0.00	0.59	0.14	0.27	Barlens
UGC02403	0.0133	10.422	Sb	0.86	20.7	1.04	0.62	0.46 ± 0.01	0.286 ± 0.007	148.4 ± 0.7	140.8 ± 0.4	$0.39^{0.64}_{0.21}$	$0.24^{0.29}_{0.09}$	0.00	0.36	0.01	0.63	None
NGC 1645	0.0160	10.673	S0a	0.12	19.6	0.95	0.60	0.48 ± 0.01	0.618 ± 0.007	86.5 ± 0.7	22.9 ± 0.4	$0.39^{0.41}_{0.21}$	$0.54^{0.89}_{0.16}$	0.00	0.47	0.52	0.01	Barlens
NGC 1666	0.0090	10.496	S0a	0.74	19.7	1.94	0.31	0.879 ± 0.004	0.389 ± 0.003	147.5 ± 0.3	141.5 ± 0.2	$0.36^{0.44}_{0.19}$	$0.46^{0.74}_{0.16}$	0.00	0.47	0.46	0.08	None
NGC 1667	0.0149	10.620	Sbc	0.72	18.4	1.48	0.29	0.687 ± 0.007	0.483 ± 0.006	172.1 ± 0.3	11.8 ± 0.2	$0.54^{0.59}_{0.29}$	$0.34^{0.59}_{0.16}$	0.00	0.51	0.17	0.32	None
UGC03253	0.0145	10.390	Sb	0.66	19.7	1.02	0.42	0.60 ± 0.01	0.295 ± 0.007	78.4 ± 0.7	35.8 ± 0.4	$0.21^{0.24}_{0.09}$	$0.21^{0.34}_{0.09}$	0.00	0.80	0.15	0.05	Barlens
UGC03995	0.0164	10.773	Sb	0.67	20.0	2.03	0.67	0.526 ± 0.007	0.313 ± 0.006	93.6 ± 0.3	119.6 ± 0.2	$0.31^{0.36}_{0.14}$	$0.19^{0.31}_{0.06}$	0.00	0.78	0.05	0.17	Barlens
NGC 2486	0.0161	10.483	Sab	0.24	20.7	2.06	0.55	0.591 ± 0.009	0.425 ± 0.007	90.7 ± 0.5	49.8 ± 0.4	$0.31^{0.36}_{0.14}$	$0.34^{0.51}_{0.09}$	0.00	0.72	0.21	0.06	Barlens
UGC04145	0.0161	10.548	Sa	0.70	20.3	1.09	0.42	0.50 ± 0.01	0.418 ± 0.007	138.2 ± 0.7	130.4 ± 0.4	$0.71^{0.76}_{0.39}$	$0.21^{0.41}_{0.06}$	0.00	0.25	0.02	0.73	None
UGC04195	0.0170	10.186	Sb	0.51	20.4	1.23	0.53	0.590 ± 0.009	0.259 ± 0.007	13.2 ± 0.5	151.0 ± 0.4	$0.19^{0.21}_{0.09}$	$0.19^{0.29}_{0.06}$	0.00	0.83	0.13	0.04	Barlens
NGC 2530	0.0174	9.988	Sd	0.30	20.6	1.86	1.03	0.84 ± 0.01	0.33 ± 0.01	156.3 ± 0.7	38.9 ± 0.4	$0.26^{0.29}_{0.14}$	$0.59^{1.01}_{0.19}$	0.10	0.24	0.65	0.01	None
NGC 2543	0.0091	10.036	Sbc	0.61	20.1	1.39	0.38	0.583 ± 0.007	0.348 ± 0.006	46.0 ± 0.3	91.8 ± 0.2	$0.24^{0.26}_{0.09}$	$0.26^{0.41}_{0.09}$	0.00	0.77	0.18	0.04	Barlens?
UGC04308	0.0127	10.081	Sc	0.31	20.5	3.40	0.57	0.740 ± 0.009	0.190 ± 0.007	126.6 ± 0.5	96.8 ± 0.4	$0.16^{0.21}_{0.09}$	$0.19^{0.26}_{0.06}$	0.00	0.84	0.12	0.03	None
NGC 2553	0.0165	10.665	Sb	0.79	20.2	1.66	0.72	0.59 ± 0.01	0.511 ± 0.007	59.5 ± 0.7	11.3 ± 0.4	$0.36^{0.39}_{0.16}$	$0.41^{0.66}_{0.14}$	0.00	0.61	0.34	0.04	Barlens
NGC 2558	0.0174	10.722	Sb	0.66	20.1	1.61	0.65	0.67 ± 0.01	0.429 ± 0.007	157.4 ± 0.7	167.8 ± 0.4	$0.46^{0.61}_{0.26}$	$0.39^{0.51}_{0.11}$	0.00	0.49	0.10	0.41	None
NGC 2565	0.0127	10.605	Sb	0.63	19.5	1.49	0.46	0.501 ± 0.007	0.386 ± 0.006	166.3 ± 0.3	176.8 ± 0.2	$0.61^{0.66}_{0.36}$	$0.21^{0.36}_{0.06}$	0.00	0.35	0.03	0.62	BP?
NGC 2880	0.0066	10.308	E7	0.72	19.9	2.86	1.06	0.571 ± 0.003	0.541 ± 0.003	143.2 ± 0.1	81.5 ± 0.1	$0.36^{0.36}_{0.19}$	$0.51^{0.89}_{0.16}$	0.00	0.43	0.55	0.02	None
NGC 3300	0.0117	10.475	S0a	0.77	19.1	1.25	0.40	0.551 ± 0.007	0.420 ± 0.006	174.6 ± 0.3	43.7 ± 0.2	$0.26^{0.29}_{0.11}$	$0.34^{0.51}_{0.09}$	0.00	0.71	0.25	0.04	Barlens
NGC 3811	0.0119	10.321	Sbc	0.57	19.4	0.73	0.29	0.668 ± 0.007	0.570 ± 0.006	12.9 ± 0.3	30.3 ± 0.2	$0.66^{0.71}_{0.46}$	$0.36^{0.61}_{0.11}$	0.00	0.42	0.14	0.45	None
NGC 4003	0.0235	10.946	S0a	0.75	20.8	1.44	1.51	0.70 ± 0.01	0.271 ± 0.007	175.4 ± 0.7	143.6 ± 0.4	$0.24^{0.29}_{0.11}$	$0.24^{0.36}_{0.09}$	0.00	0.78	0.15	0.08	Barlens
NGC 4185	0.0148	10.427	Sbc	-0.43	20.2	1.01	0.66	0.666 ± 0.004	0.796 ± 0.003	166.9 ± 0.3	172.1 ± 0.2	$0.94^{0.96}_{0.84}$	$0.64^{0.76}_{0.49}$	0.00	0.09	0.04	0.88	None
NGC 4210	0.0105	10.153	Sb	0.49	19.9	0.82	0.32	0.731 ± 0.004	0.274 ± 0.003	94.09 ± 0.3	47.4 ± 0.23	$0.21^{0.24}_{0.11}$	$0.26^{0.44}_{0.11}$	0.00	0.68	0.29	0.03	Barlens
NGC 5157	0.0263	11.021	Sab	0.68	20.2	1.21	1.61	0.78 ± 0.01	0.320 ± 0.007	105.7 ± 0.7	144.1 ± 0.4	$0.26^{0.31}_{0.11}$	$0.34^{0.54}_{0.11}$	0.00	0.61	0.35	0.04	None
NGC 5205	0.0075	9.8618	Sbc	0.53	19.6	0.86	0.28	0.63 ± 0.01	0.335 ± 0.007	152.6 ± 0.7	104.7 ± 0.4	$0.24^{0.26}_{0.11}$	$0.26^{0.44}_{0.09}$	0.00	0.72	0.24	0.03	BP
UGC08781	0.0274	10.871	Sb	0.63	20.2	2.13	0.99	0.60 ± 0.01	0.274 ± 0.007	165.9 ± 0.7	172.6 ± 0.4	$0.36^{0.46}_{0.14}$	$0.21^{0.31}_{0.09}$	0.00	0.62	0.04	0.34	None
NGC 5378	0.0121	10.140	Sb	0.17	20.9	2.51	0.82	0.74 ± 0.03	0.31 ± 0.03	80 ± 2.3	40.0 ± 1.7	$0.24^{0.31}_{0.11}$	$0.34^{0.49}_{0.11}$	0.00	0.67	0.29	0.04	Barlens
NGC 5406	0.0192	11.017	Sb	0.40	19.9	1.30	0.63	0.771 ± 0.004	0.293 ± 0.003	120.0 ± 0.3	53.5 ± 0.3	$0.19^{0.24}_{0.11}$	$0.64^{0.84}_{0.21}$	0.00	0.27	0.73	0.01	None
NGC 5520	0.0081	9.7922	Sbc	0.44	19.5	–	–	0.56 ± 0.01	0.531 ± 0.006	65 ± 1.0	65.3 ± 0.5	$1.00^{1.00}_{0.94}$	$0.24^{0.36}_{0.04}$	0.00	0.02	0.00	0.98	None
NGC 5519	0.0271	10.660	Sb	0.49	20.3	3.24	2.12	0.71 ± 0.02	0.46 ± 0.02	75.9 ± 0.9	105.9 ± 0.8	$0.44^{0.49}_{0.21}$	$0.36^{0.61}_{0.11}$	0.00	0.58	0.26	0.16	None
IC0994	0.0269	11.072	S0a	0.80	19.8	2.16	0.87	0.51 ± 0.01	0.481 ± 0.007	14.6 ± 0.7	29.2 ± 0.4	$0.59^{0.66}_{0.31}$	$0.34^{0.49}_{0.09}$	0.00	0.41	0.05	0.54	None

Table A1 – *continued*

Galaxy	Redshift	$\log(M_\star/M_\odot)$	HT	$g-r$ (disc)	μ_0	n	r_e	q_d	q_{bar}	PA_d	PA_{bar}	B/A	C/A	P(pro. o)	P(pro. i)	P(obl. o)	P(obl. i)	V. class
(1)	(2)	(3)	(4)	(5)	(6)	(7)	(8)	(9)	(10)	(11)	(12)	(13)	(14)	(15)	(16)	(17)	(18)	(19)
NGC 5602	0.0092	10.322	S0a	4.92	20.8	2.39	0.46	0.52 ± 0.03	0.59 ± 0.03	167 ± 2.3	165.1 ± 1.7	$0.94^{1.00}_{0.81}$	$0.41^{0.51}_{0.26}$	0.00	0.05	0.01	0.94	None
UGC09291	0.0116	9.6661	Scd	0.44	20.4	1.06	0.41	0.514 ± 0.009	0.319 ± 0.007	107.2 ± 0.5	73.0 ± 0.4	$0.24^{0.29}_{0.09}$	$0.21^{0.31}_{0.06}$	0.00	0.82	0.08	0.10	None
NGC 5735	0.0145	10.127	Sbc	0.45	20.3	1.20	0.42	0.90 ± 0.01	0.223 ± 0.007	32.6 ± 0.7	94.9 ± 0.4	$0.16^{0.21}_{0.06}$	$0.64^{0.96}_{0.21}$	0.02	0.19	0.79	0.00	None
UGC09492	0.0299	11.082	Sab	0.78	20.1	1.58	1.37	0.45 ± 0.01	0.420 ± 0.007	54.2 ± 0.7	80.8 ± 0.4	$0.36^{0.44}_{0.16}$	$0.26^{0.39}_{0.06}$	0.00	0.77	0.06	0.17	Barlens?
IC4534	0.0185	10.723	S0a	0.48	20.0	2.10	0.85	0.564 ± 0.009	0.293 ± 0.007	162.9 ± 0.5	179.1 ± 0.4	$0.31^{0.44}_{0.16}$	$0.24^{0.31}_{0.06}$	0.00	0.68	0.04	0.28	BP
NGC 5876	0.0126	10.678	S0a	0.69	20.6	1.57	0.72	0.433 ± 0.004	0.483 ± 0.003	52.4 ± 0.3	179.4 ± 0.2	$0.24^{0.26}_{0.11}$	$0.31^{0.48}_{0.11}$	0.00	0.76	0.22	0.02	Barlens
NGC 5888	0.0308	11.135	Sb	0.61	19.8	1.40	1.06	0.596 ± 0.009	0.243 ± 0.007	153.2 ± 0.5	170.5 ± 0.4	$0.31^{0.34}_{0.14}$	$0.14^{0.26}_{0.09}$	0.00	0.75	0.05	0.20	BP
NGC 6154	0.0216	10.744	Sab	0.64	20.5	2.32	1.15	0.79 ± 0.01	0.250 ± 0.007	135.9 ± 0.7	135.4 ± 0.4	$0.24^{0.31}_{0.11}$	$0.26^{0.36}_{0.11}$	0.00	0.79	0.14	0.08	Barlens?
NGC 6278	0.0111	10.719	S0a	0.69	20.0	2.31	0.64	0.530 ± 0.004	0.379 ± 0.003	126.8 ± 0.3	116.0 ± 0.2	$0.54^{0.64}_{0.34}$	$0.26^{0.36}_{0.09}$	0.00	0.42	0.03	0.55	None
NGC 6497	0.0217	10.865	Sab	0.58	20.1	3.33	1.11	0.495 ± 0.009	0.392 ± 0.007	111.2 ± 0.5	160.8 ± 0.4	$0.21^{0.26}_{0.09}$	$0.29^{0.41}_{0.09}$	0.00	0.79	0.18	0.03	Barlens
UGC11228	0.0206	10.867	S0	0.81	20.3	2.50	1.14	0.67 ± 0.01	0.286 ± 0.007	176.2 ± 0.7	157.5 ± 0.4	$0.31^{0.36}_{0.14}$	$0.21^{0.34}_{0.11}$	0.00	0.77	0.08	0.14	None
NGC 6941	0.0216	10.885	Sb	0.66	20.2	1.76	0.85	0.72 ± 0.01	0.248 ± 0.007	130.5 ± 0.7	109.1 ± 0.4	$0.26^{0.29}_{0.14}$	$0.19^{0.31}_{0.11}$	0.00	0.79	0.12	0.09	BP?
NGC 6945	0.0136	10.946	S0	0.74	19.9	3.74	1.09	0.649 ± 0.007	0.507 ± 0.006	120.2 ± 0.3	86.7 ± 0.2	$0.46^{0.51}_{0.21}$	$0.36^{0.64}_{0.14}$	0.00	0.60	0.24	0.16	Barlens?
NGC 7321	0.0238	10.691	Sbc	0.59	19.3	1.79	0.53	0.65 ± 0.01	0.412 ± 0.007	22.2 ± 0.7	71.7 ± 0.4	$0.29^{0.34}_{0.14}$	$0.39^{0.61}_{0.11}$	0.00	0.60	0.36	0.04	Barlens
NGC 7563	0.0139	10.720	Sa	0.71	21.5	2.47	1.21	0.513 ± 0.009	0.392 ± 0.007	151.5 ± 0.5	91.9 ± 0.4	$0.21^{0.24}_{0.09}$	$0.29^{0.51}_{0.11}$	0.00	0.66	0.33	0.01	Barlens
NGC 7591	0.0164	10.610	Sbc	0.68	20.3	2.30	2.00	0.48 ± 0.01	0.484 ± 0.007	148.4 ± 0.7	10.5 ± 0.4	$0.31^{0.34}_{0.14}$	$0.31^{0.48}_{0.09}$	0.00	0.78	0.17	0.05	None
NGC 7611	0.0109	10.721	S0	0.84	18.8	1.66	0.28	0.487 ± 0.007	0.711 ± 0.006	137.0 ± 0.3	1.7 ± 0.2	$0.51^{0.54}_{0.26}$	$0.56^{0.81}_{0.19}$	0.00	0.63	0.33	0.04	None
NGC 7623	0.0125	10.565	S0	0.90	20.6	1.90	1.02	0.719 ± 0.009	0.400 ± 0.007	7.0 ± 0.5	161.1 ± 0.4	$0.39^{0.46}_{0.19}$	$0.34^{0.54}_{0.09}$	0.00	0.64	0.21	0.15	None
NGC 7671	0.0137	10.655	S0	0.88	18.8	1.76	0.48	0.596 ± 0.004	0.617 ± 0.003	135.1 ± 0.3	24.0 ± 0.2	$0.46^{0.49}_{0.29}$	$0.66^{1.21}_{0.26}$	0.31	0.26	0.41	0.01	None
NGC 7691	0.0134	10.176	Sbc	0.52	20.5	1.38	0.56	0.78 ± 0.01	0.361 ± 0.007	160.0 ± 0.7	2.7 ± 0.4	$0.36^{0.42}_{0.16}$	$0.31^{0.54}_{0.11}$	0.00	0.62	0.27	0.11	None
NGC 7716	0.0087	10.289	Sb	0.52	19.7	2.87	0.31	0.822 ± 0.008	0.514 ± 0.002	39.4 ± 0.4	15.7 ± 0.2	$0.49^{0.56}_{0.29}$	$0.51^{0.81}_{0.16}$	0.00	0.45	0.39	0.16	None
UGC04455	0.0310	10.878	Sb	-0.20	20.3	0.97	0.81	0.74 ± 0.03	0.23 ± 0.03	11 ± 2.3	165 ± 1.7	$0.21^{0.26}_{0.09}$	$0.21^{0.33}_{0.06}$	0.00	0.80	0.14	0.06	Barlens?
UGC05187	0.0049	8.7767	Sdm	0.05	20.6	–	–	0.825 ± 0.008	0.392 ± 0.008	133.8 ± 1.6	79.9 ± 0.7	$0.31^{0.36}_{0.14}$	$0.59^{0.94}_{0.19}$	0.01	0.32	0.65	0.02	None
UGC05377	0.0071	8.8268	Sdm	0.39	21.1	–	–	0.835 ± 0.008	0.321 ± 0.006	77.6 ± 1.5	135.1 ± 0.7	$0.24^{0.29}_{0.11}$	$0.59^{0.86}_{0.16}$	0.00	0.32	0.67	0.01	None
UGC07129	0.0040	9.2663	Sab	-0.06	19.6	–	–	0.64 ± 0.01	0.164 ± 0.006	73 ± 1.0	61.6 ± 0.5	$0.19^{0.24}_{0.09}$	$0.14^{0.19}_{0.06}$	0.00	0.82	0.04	0.14	None
NGC 0495	0.0135	10.902	Sab	-0.81	19.8	1.58	0.67	0.73 ± 0.01	0.345 ± 0.007	10.4 ± 0.7	10.5 ± 0.4	$0.41^{0.46}_{0.16}$	$0.26^{0.46}_{0.14}$	0.00	0.63	0.13	0.23	None
KUG1349+143	0.0247	10.076	Sbc	-0.05	20.9	1.65	0.26	0.63 ± 0.03	0.23 ± 0.04	96 ± 2.3	96 ± 1.3	$0.29^{0.41}_{0.11}$	$0.19^{0.29}_{0.06}$	0.00	0.71	0.04	0.24	None
IC1078	0.0287	10.645	Sb	0.08	20.7	1.92	0.60	0.82 ± 0.02	0.27 ± 0.02	99.5 ± 0.9	100.1 ± 0.8	$0.26^{0.34}_{0.11}$	$0.29^{0.44}_{0.11}$	0.00	0.72	0.21	0.07	None
NGC 0515	0.0170	11.038	E7	-0.25	19.9	1.77	0.54	0.77 ± 0.01	0.466 ± 0.007	103.9 ± 0.7	131.9 ± 0.4	$0.46^{0.51}_{0.26}$	$0.36^{0.66}_{0.11}$	0.00	0.54	0.32	0.15	Barlens?
NGC 2780	0.0068	9.5927	Sbc	-0.17	20.2	0.56	0.16	0.721 ± 0.009	0.166 ± 0.007	143.7 ± 0.5	113.9 ± 0.4	$0.14^{0.19}_{0.06}$	$0.16^{0.21}_{0.06}$	0.00	0.85	0.10	0.05	None
UGC06517	0.0084	9.3464	Sc	0.16	19.5	–	–	0.60 ± 0.01	0.287 ± 0.008	34.4 ± 1.5	105.6 ± 0.8	$0.16^{0.16}_{0.06}$	$0.36^{0.64}_{0.11}$	0.00	0.39	0.61	0.00	None
UGC12250	0.0240	11.106	Sbc	0.22	20.7	1.15	0.71	0.626 ± 0.009	0.320 ± 0.007	12.7 ± 0.5	13.3 ± 0.4	$0.34^{0.54}_{0.19}$	$0.31^{0.36}_{0.09}$	0.00	0.55	0.05	0.40	None
NGC 5947	0.0198	10.559	Sbc	0.39	20.6	2.71	0.61	0.811 ± 0.009	0.294 ± 0.007	63.7 ± 0.5	25.7 ± 0.4	$0.24^{0.29}_{0.11}$	$0.36^{0.54}_{0.14}$	0.00	0.59	0.38	0.04	Barlens
UGC03552	0.0160	10.067	Sd	0.46	20.3	–	–	0.46 ± 0.01	0.475 ± 0.008	78.3 ± 1.5	96.3 ± 0.8	$0.51^{0.59}_{0.24}$	$0.34^{0.46}_{0.11}$	0.00	0.57	0.05	0.38	None
NGC 3323	0.0173	9.8078	Scd	0.39	19.3	–	–	0.495 ± 0.008	0.161 ± 0.006	157.1 ± 1.5	163.9 ± 0.7	$0.21^{0.34}_{0.09}$	$0.14^{0.16}_{0.06}$	0.00	0.63	0.01	0.36	None
NGC 2767	0.0165	10.750	S0	0.83	18.9	1.22	0.33	0.733 ± 0.009	0.417 ± 0.007	169.6 ± 0.5	150.7 ± 0.4	$0.44^{0.51}_{0.24}$	$0.34^{0.54}_{0.11}$	0.00	0.59	0.19	0.22	None

Note. (1) Galaxy name; (2), (3), and (4) redshift, galaxy stellar mass, and galaxy Hubble type from Walcher et al. (2014); (5), (6) integrated disc $g-r$ colour and central surface brightness of the disc; (7) and (8) Sérsic index and effective radius (in kpc) of the bulge; (9) and (10) apparent axial ratios of the disc and the bar, (11) and (12) position angle of the disc and the bar, (13) and (14) most probable intrinsic axial ratios *B/A* and *C/A* of the bar, the 1σ probability values for each case are also shown; (15), (16), (17) and (18) probability for a given bar to prolate off-plane (pro. o), prolate in-plane (pro. i), oblate off-plane (obl. o), and oblate in-plane (obl. i), respectively; (19) visual classification to detect inner boxy/peanuts structures (see text for an explanation of the different classes). Columns (5, 6, 7, 8, 9, 10, 11, 12) are from (Méndez-Abreu et al. 2017).

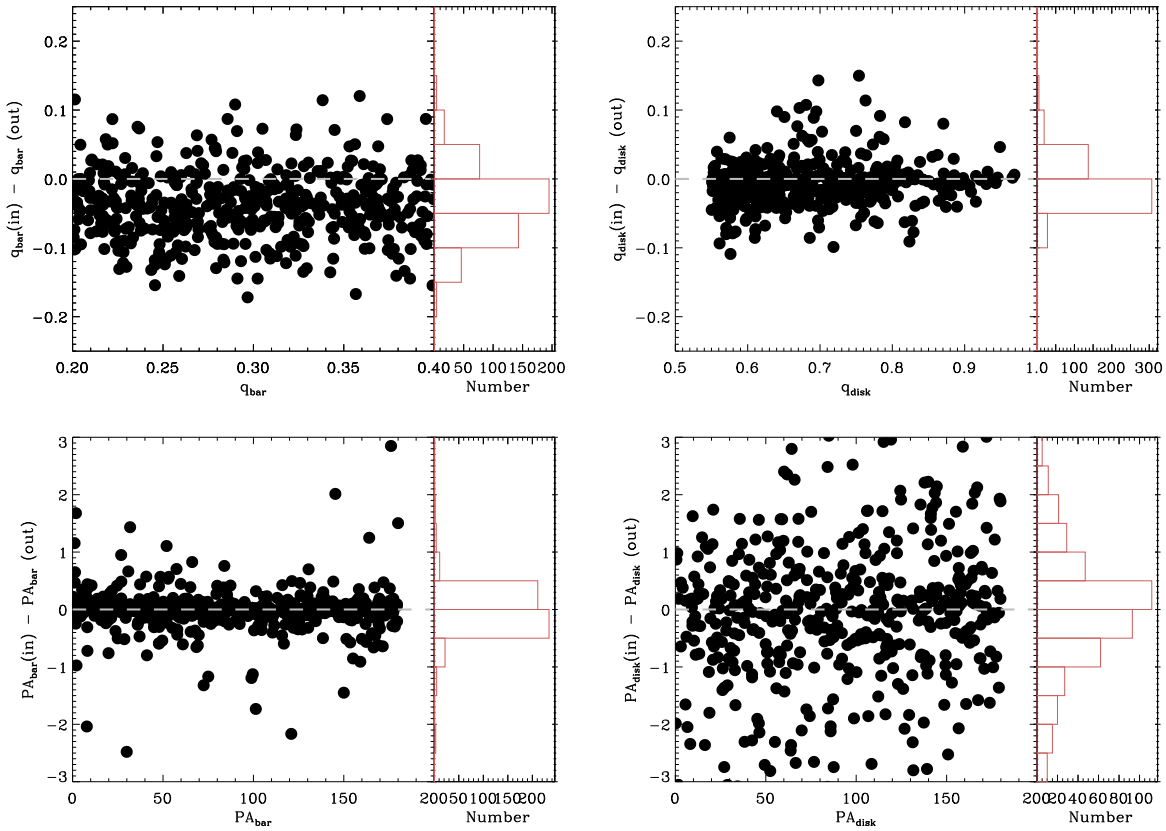

Figure B1. Differences between the input and output values obtained from our mock galaxy simulations including barlenses for the parameters involved in our analysis: bar axis ratio (upper left), disc axis ratio (upper right), bar position angle (bottom left), disc position angle (bottom right). The histograms of the differences are also shown.

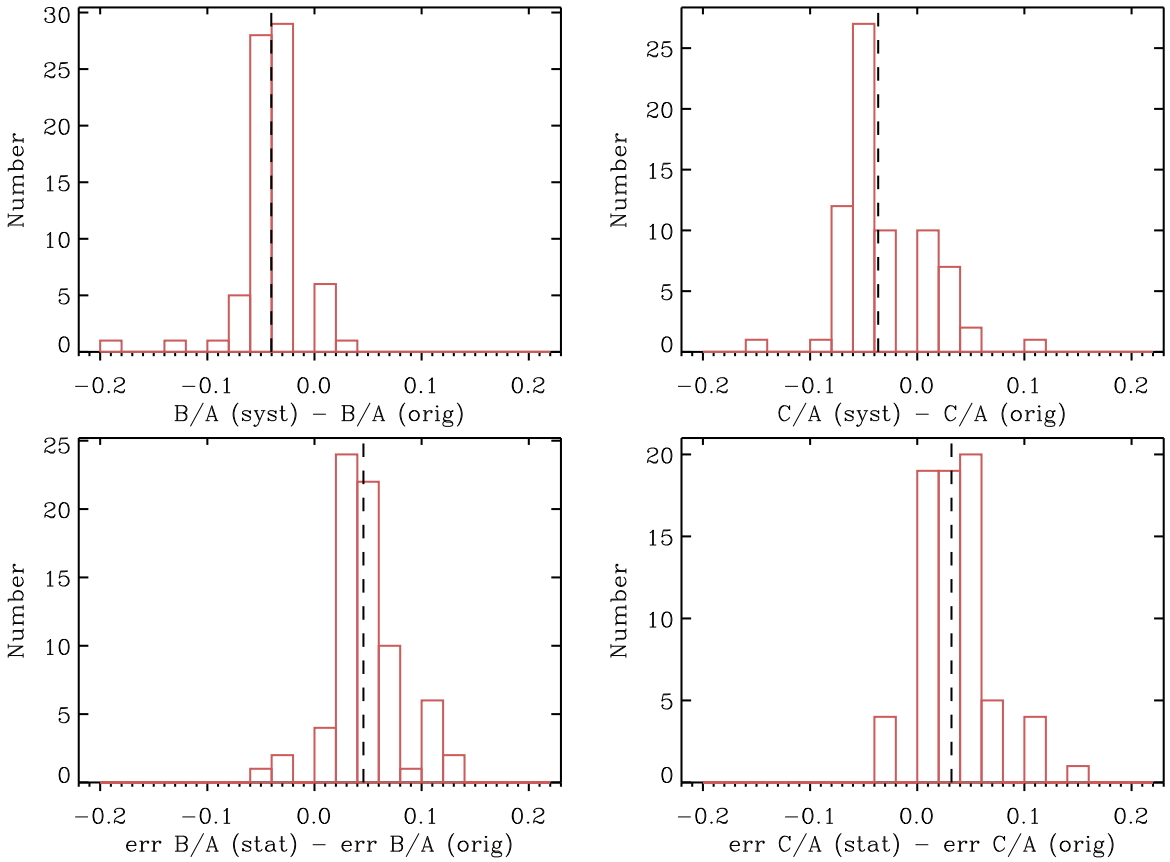

Figure B2. *Top panels.* Distribution of differences between the derived values of the intrinsic *B*/*A* and *C*/*A* of bars correcting for the systematic (syst) error on the observational parameters due to the presence of a barlens structure and those obtained in this paper (orig). *Bottom panels.* Distribution of differences between the derived uncertainties in the intrinsic *B*/*A* and *C*/*A* semiaexes of bars assuming the statistical (stat) error on the observational parameters due to the presence of a barlens structure and those obtained in this paper (orig).

This paper has been typeset from a TEX/LATEX file prepared by the author.